



# Conservation of the Direct and Indirect Pathway Dichotomy in Mouse Caudal Striatum With Uneven Distribution of Dopamine Receptor D1- and D2-Expressing Neurons

## OPEN ACCESS

**Kumiko Ogata<sup>1</sup>, Fuko Kadono<sup>2</sup>, Yasuharu Hirai<sup>1,2</sup>, Ken-ichi Inoue<sup>3</sup>, Masahiko Takada<sup>3</sup>, Fuyuki Karube<sup>1,2\*†</sup> and Fumino Fujiyama<sup>1,2\*†</sup>**

### Edited by:

Savio Chan,  
Northwestern Medicine, United States

### Reviewed by:

Emmanuel Valjent,  
Centre National de la Recherche  
Scientifique (CNRS), France  
Charles J. Wilson,  
University of Texas at San Antonio,  
United States  
Qiaojie Xiong,  
Stony Brook University, United States  
Giuseppe Gangarossa,  
Université de Paris, France

Megan Fox,  
Penn State College of Medicine,  
United States

### \*Correspondence:

Fuyuki Karube  
karube@med.hokudai.ac.jp  
Fumino Fujiyama  
fujiyama@pop.med.hokudai.ac.jp

†These authors share senior and last authorship

**Received:** 05 November 2021

**Accepted:** 04 January 2022

**Published:** 04 February 2022

### Citation:

Ogata K, Kadono F, Hirai Y, Inoue K-i, Takada M, Karube F and Fujiyama F (2022) Conservation of the Direct and Indirect Pathway Dichotomy in Mouse Caudal Striatum With Uneven Distribution of Dopamine Receptor D1- and D2-Expressing Neurons.

Front. Neuroanat. 16:809446.  
doi: 10.3389/fnana.2022.809446

<sup>1</sup> Laboratory of Neural Circuitry, Graduate School of Brain Science, Doshisha University, Kyotanabe, Japan, <sup>2</sup> Laboratory of Histology and Cytology, Faculty of Medicine and Graduate School of Medicine, Hokkaido University, Sapporo, Japan, <sup>3</sup> Systems Neuroscience Section, Primate Research Institute, Kyoto University, Inuyama, Japan

The striatum is one of the key nuclei for adequate control of voluntary behaviors and reinforcement learning. Two striatal projection neuron types, expressing either dopamine receptor D1 (D1R) or dopamine receptor D2 (D2R) constitute two independent output routes: the direct or indirect pathways, respectively. These pathways co-work in balance to achieve coordinated behavior. Two projection neuron types are equivalently intermingled in most striatal space. However, recent studies revealed two atypical zones in the caudal striatum: the zone in which D1R-neurons are the minor population (D1R-poor zone) and that in which D2R-neurons are the minority (D2R-poor zone). It remains obscure as to whether these imbalanced zones have similar properties on axonal projections and electrophysiology compared to other striatal regions. Based on morphological experiments in mice using immunofluorescence, *in situ* hybridization, and neural tracing, here, we revealed that the poor zones densely projected to the globus pallidus and substantia nigra pars lateralis, with a few collaterals in substantia nigra pars reticulata and compacta. Similar to that in other striatal regions, D1R-neurons were the direct pathway neurons. We also showed that the membrane properties of projection neurons in the poor zones were largely similar to those in the conventional striatum using *in vitro* electrophysiological recording. In addition, the poor zones existed irrespective of the age or sex of mice. We also identified the poor zones in the common marmoset as well as other rodents. These results suggest that the poor zones in the caudal striatum follow the conventional projection patterns irrespective of the imbalanced distribution of projection neurons. The poor zones could be an innate structure and common in mammals. The unique striatal zones possessing highly restricted projections could relate to functions different from those of motor-related striatum.

**Keywords:** striatum, substantia nigra pars lateralis, dopamine receptor, tyrosine hydroxylase, basal ganglia, direct pathway, indirect pathway

## INTRODUCTION

The striatum regulates voluntary movement and reward-related learning by integrating excitatory inputs from the cerebral cortex and thalamus (Alexander et al., 1986; Hikosaka et al., 2000; Kreitzer and Malenka, 2008; Redgrave et al., 2011; Peak et al., 2019). The medium spiny projection neurons (MSNs)—i.e., the major population of striatal neurons—are classified into two groups: direct and indirect pathway neurons, depending on their projection targets and gene expression. The direct pathway MSNs (dMSNs) directly transmit information to output nuclei, such as the globus pallidus internal segment (GPi) [the counter part of the entopeduncular nucleus (EP) in rodents] and substantia nigra (SN). The dMSNs express gamma-aminobutyric acid (GABA), dopamine receptor D1 (D1R), and substance P. In contrast, indirect pathway MSNs (iMSNs) express GABA, dopamine receptor D2 (D2R), and enkephalin, and project to the globus pallidus external segment (GP in rodents). In turn, GP projects to the output nuclei, namely, iMSNs indirectly project to the output nuclei (Albin et al., 1989; Alexander and Crutcher, 1990; Graybiel, 1990). It has long been believed that both types of projection neurons are randomly distributed (Lança et al., 1986; Gerfen, 1989; Tinterri et al., 2018) and each local striatal area contains an almost equal proportion of both types (Selemon and Goldman-Rakic, 1990; Hedreen and DeLong, 1991).

Dense and topographic corticostriatal innervation recruits striatal subregions for specific functions (Nambu, 2008; Shepherd, 2013; Shipp, 2016). The caudal striatum (cStr) in rodents lies under the temporal cortical area as being similar to the caudate tail (CDt) in primates, which is a curved long extension of the ventral part of the caudate nucleus. Temporal areas, including somatosensory, visual, and auditory related areas, innervate cStr in rodents (Deniau et al., 1996; Xiong et al., 2015; Hintiryan et al., 2016; Hunnicutt et al., 2016; Jiang and Kim, 2018; Foster et al., 2021) and CDt in primates (Yeterian and Van Hoesen, 1978; Caan et al., 1984; Saint-Cyr et al., 1990; Brown et al., 1995; Yeterian and Pandya, 1998); therefore, they are considered the sensory striatum. In addition, similar to cStr in rodents (Watabe-Uchida et al., 2012; Menegas et al., 2015), CDt in primates receives the projection from a specific group of dopaminergic neurons (Kim and Hikosaka, 2013; Kim et al., 2014). Thus, cStr in rodents and CDt in primates share common neural connection features. The functional significance of CDt and cStr has been also gradually uncovered. CDt in primates is involved in distinct functions, such as coding the value of objects (Kim and Hikosaka, 2013; Kim et al., 2014, 2017; Griggs et al.,

2017). Recent studies in rodents have shown that the cStr is involved in the avoidance behavior of mice (Menegas et al., 2017, 2018).

Gangarossa et al. (2013b) revealed a unique cStr region adjacent to GP using bacterial artificial chromosome (BAC) transgenic mice that express eGFP. The region is surprisingly composed almost exclusively of *Drd1a* expressing neurons and is therefore called D2R/A2aR-expressing MSNs-poor zone (Gangarossa et al., 2013b). Studies with transgenic mice also showed the area with fewer D1R-expressing neurons in the cStr (Miyamoto et al., 2018, 2019; for review, see Valjent and Gangarossa, 2021). Our previous study with wild-type mice also confirmed the highly uneven distribution of D1R and D2R immunoreaction in the unique regions of cStr (Ogata et al., 2018).

Although such uneven distribution of D1R and D2R immunoreactivity conjures up the possibility that the direct and indirect pathway neurons are separately distributed in the unique region of cStr, it contradicts the conservative model according to which the physiological function requires a balance of the direct and indirect pathway neurons mediated by D1R and D2R, respectively (Cui et al., 2013; Isomura et al., 2013; Calabresi et al., 2014; Friend and Kravitz, 2014). Thus, we raise two questions: first, does the uneven distribution of D1R and D2R immunoreactions actually reflect the separate distribution of the direct and indirect pathway projection neurons? If so, what are neural circuitries driven by? Second, is this uneven distribution a common property of the sensory-related striatum and conserved among rodents and primates, or is it a rodent-specific feature (Gangarossa et al., 2019)? If the former is true, sensory inputs may modify the uneven structure of the sensory-related striatum. Thus, the uneven structure may vary developmentally, since neonatal mice do not respond to visual and auditory stimuli (Huberman et al., 2008; Sonntag et al., 2009), while aged C57BL6 mice typically have impaired hearing (Zheng et al., 1999). Alternatively, the uneven structure of the cStr can be innate, although maturation of MSNs continues in the early postnatal days (Krajieski et al., 2019). To address these questions, we employed a combination of *in situ* hybridization, immunohistochemistry, electrophysiological recording, and retrograde/anterograde tracing in mice, and also compared the cStr structure across ages and species.

## MATERIALS AND METHODS

All animal experiments in mice and rats were approved by and performed in accordance with the guidelines for the care and use of laboratory animals established by the Committee for Animal Care and Use of Doshisha University (Approval number: A16008, A17001, A18001, A19036, and A20057) and the Animal Care and Use Committee of Hokkaido University (Approval Number: 20-0106). All animal studies in the common marmosets were conducted in accordance with experimental procedure protocols approved by the Animal Welfare and Animal Care Committee of the Primate Research Institute of Kyoto University (Approval number: 2017-031). All efforts were made to minimize

**Abbreviations:** ACSF, artificial cerebrospinal fluid; AP, antero-posterior; AST, amygdala-striatal transition area; Au, auditory area; BDA, biotinylated dextran amine; CDt, caudate tail; cStr, caudal striatum; cdStr, caudo-dorsal striatum; CTB, cholera toxin subunit B; DAT, dopamine transporter; dStr, dorsal striatum; D1R, dopamine receptor D1; D2R, dopamine receptor D2; EP, entopeduncular nucleus; FG, fluorogold; GP, globus pallidus; MG, medial geniculate nucleus; MSN, medium spiny neuron; PB, phosphate buffer; PBS, phosphate buffered saline; PHAL, phaseolus vulgaris leucoagglutinin; ppz, para-poor zone; rStr, rostral striatum; RT, room temperature; SNpc, substantia nigra pars compacta; SNpl, substantia nigra pars lateralis; SNpr, substantia nigra pars reticulata; SubB, subbrachial nucleus; TH, tyrosine hydroxylase; VPM, ventral posterior nucleus of thalamus, the medial part; VPL, ventral posterior nucleus of thalamus, the lateral part.

animal suffering and the number of animals used. Chemicals were purchased from Nacalai Tesque (Kyoto, Japan) and Wako (Osaka, Japan) unless otherwise noted.

In this study, 42 wild-type C57BL/6J male mice (8-day-old to 172-week-old), three wild-type slc:ICR male mice (11-week-old), three Long-Evans male rats (11–13-week-old), three Wistar male rats (12-week-old), and two common marmosets (a 6.8-year-old male and a 5.2-year-old female) were utilized. Additionally, three female BL6 mice were also used to examine sexual differences (10–12-week-old).

## Animal Surgery: Retro- and Anterograde Tracing Study

Mice were anesthetized by inhalation of isoflurane (Pfizer Japan Inc., Tokyo, Japan) followed by intramuscular injection of a mixture of ketamine (Ketalar; Daiichi-Sankyo, Tokyo, Japan; 40 mg/kg) and xylazine (Bayer HealthCare, Tokyo, Japan; 4 mg/kg). Before and after surgery, butorphanol solution (Meiji Seika Pharma Co Ltd, Tokyo, Japan) was injected subcutaneously (0.2 mg/kg) for analgesia. Each mouse was then fixed to a stereotaxic device (Narishige, Tokyo, Japan). During surgery, the body temperature of the mice was monitored and maintained at approximately 38°C (BWT 100A animal warmer; Bio Research Center, Nagoya, Japan). The skull was drilled to make a small hole at an appropriate position in accordance with the mouse brain atlas (Paxinos and Franklin, 2013). For the retrograde labeling of projection neurons in the rostral and caudal striatum simultaneously, a large volume (>0.5  $\mu$ L) of 0.2% cholera toxin subunit B – Alexa Fluor 555 (CTB555) or 488 (CTB488) conjugate (C22843 or C-22841, Thermo Fisher Scientific, Inc., Waltham, MA, United States) in 0.1 M phosphate buffer (PB, pH 7.4) was injected around the output nuclei of the basal ganglia of three mice [anteroposterior (AP): 2.8 mm caudal from the bregma (AP –2.8), lateromedial: 2.1 mm lateral from the midline (L 2.1), depth: 3.7–4.2 mm from the pial surface (D 3.7–4.2)] using a glass pipette (tip diameter, 15–20  $\mu$ m) through which air pressure pulses were delivered with a pressure injector (PV820, World Precision Instruments, Sarasota, FL, United States). The site of injection extended to the substantia nigra pars reticulata (SNpr), substantia nigra pars compacta (SNpc), and EP, but did not reach the GP. For the retrograde tracing from the substantia nigra pars lateralis (SNpl) or medial geniculate nucleus (MG), 0.2% CTB555 (~0.2  $\mu$ l) was injected by pressure, or 5% fluorogold (FG) dissolved in phosphate-buffered saline (PBS, pH 7.4) was injected iontophoretically (0.8–1.0  $\mu$ A positive current pulses with a 7 s-on/off cycle for 5 min using A365, World Precision Instruments). The coordinates of the injection were [AP –2.9, L 1.8, D 3.8] for SNpl and [AP –3.2, L 2.0, D 2.8] for MG ( $N = 3$  mice for each).

For anterograde tracing, 10% biotinylated dextran amine (BDA 10kD) (D1956, Thermo Fisher Scientific, Inc., Waltham, MA, United States) in PBS, or 2.5% Phaseolus Vulgaris Leucoagglutinin (PHAL) (L-1110, Vector Laboratories, Burlingame, CA, United States) in 10 mM phosphate (pH 8.0) was injected in the cStr using a glass pipette (tip diameter, 15–25  $\mu$ m). The BDA solution was injected iontophoretically

by 1.2  $\mu$ A current pulses with a 7 s-on/off cycle for 5–20 min, or ejected by a single air pulse. PHAL was injected by 4  $\mu$ A current pulses with a 7 s-on/off cycle for 5 min. After 3–5 days, each mouse was perfused as described below. The targeted coordinates for the caudo-dorsal striatum (cdStr) were [AP –1.2, L 2.7, D 1.7], and those for D1R- and/or D2R-poor zones were [AP –1.2, L 2.7, D 2.8] as described in the mouse brain atlas (Paxinos and Franklin, 2013).

## Immunofluorescence Labeling and Tracer Visualization

### Tissue Preparation

The mice and rats were deeply anesthetized with isoflurane and sodium pentobarbital (100 mg/kg, i.p.; Kyoritsu Seiyaku Corporation, Tokyo, Japan). The animals were then transcardially perfused with 8.5% sucrose in 20 mM PB containing 5 mM MgCl<sub>2</sub>, followed by 4% w/v paraformaldehyde and 75% saturated picric acid in 0.1 M PB. After the perfusion pump was switched off, the brain was postfixed *in situ* for 1.5 h at room temperature (RT; 25  $\pm$  3°C), and then the brain was removed from the skull, followed by cryoprotection with 30% sucrose in PBS for 24–48 h at 4°C. Tissue blocks containing the striatum were sectioned sagittally or coronally using a freezing microtome (Leica Microsystems, Wetzlar, Germany) at a thickness of 20  $\mu$ m. Six series of floating sections were collected in 0.1 M PB containing 0.02% of sodium azide and prepared for immunofluorescence labeling.

Two common marmosets (*Callithrix jacchus*; one male and one female) weighing around 370 g were used for this study. They were caged at 27  $\pm$  2°C in 50  $\pm$  10% humidity with a 12-h light-dark cycle and were fed two times a day with a standard marmoset diet supplemented with fruit, mealworm, and gum with vitamin D. Water was available *ad libitum*. Following sedation with ketamine hydrochloride (40 mg/kg, i.m.), the marmosets were deeply anesthetized with an overdose of sodium pentobarbital (50 mg/kg, i.v.) for perfusion-fixation. The marmosets were transcardially perfused with 0.1 M PBS followed by 4% paraformaldehyde in 0.1 M PB. The brain was removed from the skull, postfixed in the same fresh fixative overnight, and saturated with 30% sucrose in PB at 4°C. Tissue blocks containing the putamen and caudate nucleus were sectioned coronally using a freezing microtome at a thickness of 25  $\mu$ m. Twelve series of floating sections were collected in 0.1 M PB containing 0.02% of sodium azide and prepared for immunofluorescence labeling.

### Immunofluorescence Labeling

The brain sections of the mice, rats, and marmosets were incubated with a mixture of primary antibodies overnight at RT (Table 1). The primary antibodies were diluted with incubation buffer containing 10% (v/v) normal donkey serum (Merck KGaA, Darmstadt, Germany), 2% bovine serum albumin, and 0.5% (v/v) Triton X-100 in 0.05 M Tris-buffered saline (TBS). After exposure to the primary antibodies, the sections were washed in TBS and incubated for 3 h at RT in the same buffer containing a mixture of secondary antibodies (Table 2). In some cases, the whole immunoreaction steps were repeated to enhance signals. After

**TABLE 1** | Primary antibodies used in this study.

Antigen	Host species	Dilution	Supplier catalog #	RRID
Alexa Fluor 488	Rabbit	1:2,000	Thermo Fisher Scientific A10094	AB_221544
DARPP32	Goat	1:500	Frontier Institute DARPP-Go-A1090	AB_2571684
Dopamine receptor D1	Guinea pig	1:500	Frontier Institute D1R-GP-Af500	AB_2571595
Dopamine receptor D1	Rat	1:500	Sigma Aldrich D2944	AB_10466396
Dopamine receptor D2	Guinea pig	1:500	Frontier Institute D2R-GP-Af500	AB_2571597
Dopamine receptor D2	Rabbit	1:500	Frontier Institute D2R-Rb-Af960	AB_2571596
Dopamine transporter	Goat	1:1,000	Frontier Institute DAT-Go-Af980	AB_2571687
NeuN	Mouse	1:10,000	Millipore MAB377	AB_10048713
NeuN	Rabbit	1:1,000	Millipore ABN78	AB_10807945
Parvalbumin	Guinea pig	1:4,000	Synaptic Systems 195004	AB_2156476
Phaseolus Vulgaris Agglutinin (E + L)	Goat	1:1,000	Vector AS-2224-1	AB_10000080
Tyrosine hydroxylase	Mouse	1:2,000	Millipore MAB318	AB_2313764

rinsing, the sections were mounted on glass slides, air dried, and cover-slipped with 50% (v/v) glycerol/TBS.

### Tracer Visualization

BDA was visualized with fluorophore-conjugated streptavidin (Thermo Fisher Scientific, Waltham, MA, United States **Table 2**; 1:1,000 for 3 h). The reaction was enhanced using the biotinylated tyramine (BT)-glucose oxidase (GO) amplification method (Furuta et al., 2009; Kuramoto et al., 2009; Ge et al., 2010). PHAL was detected using immunofluorescence.

### *In situ* Hybridization and NeuN Immunolabeling

All *in situ* hybridization experiments were accomplished under a ribonuclease-free condition. The mice (C57BL/6J) for *in situ* hybridization were treated as aforementioned in section “Immunofluorescence labeling and tracer visualization,” except, picric acid was excluded from the fixative. The following hybridization procedure was performed as reported previously (Hioki et al., 2010; Ma et al., 2011). Briefly, sagittal sections from both hemispheres were cut at 20- $\mu$ m thickness using a freezing microtome. Free-floating sections were hybridized for 16–20 h at 60°C with 1  $\mu$ g/ml digoxigenin (DIG)-labeled sense or antisense riboprobes in a hybridization buffer. After washes and ribonuclease A (RNase A) treatment, the sections were incubated overnight with 1:1,000 diluted alkaline phosphatase-conjugated anti-DIG sheep antibody (11-093-274-910; Roche Diagnostics, Basel, Switzerland) and

**TABLE 2** | Secondary antibodies and streptavidin used in this study.

Antibody	Host species	Dilution	Supplier catalog #	RRID
Anti-goat Alexa Fluor 546	Donkey	1:500	Thermo Fisher Scientific A11056	AB_10584485
Anti-goat Alexa Fluor 633	Donkey	1:500	Thermo Fisher Scientific A21082	AB_2535739
Anti-guinea pig Alexa Fluor 488	Donkey	1:500	Jackson Immunoresearch 706-545-148	AB_2341098
Anti-guinea pig Alexa Fluor 555	Goat	1:500	Thermo Fisher Scientific A21435	AB_2535856
Anti-guinea pig Alexa Fluor 633	Goat	1:500	Thermo Fisher Scientific A21105	AB_2535757
Anti-mouse Alexa Fluor 488	Donkey	1:500	Thermo Fisher Scientific A21202	AB_2535788
Anti-mouse Alexa Fluor 546	Donkey	1:500	Thermo Fisher Scientific A10036	AB_2534012
Anti-mouse Alexa Fluor 635	Goat	1:500	Thermo Fisher Scientific A31575	AB_2536185
Anti-rabbit biotin-SP	Donkey	1:1,000	Jackson Immunoresearch #711-065-152	AB_2340593
Anti-rabbit Alexa Fluor 488	Donkey	1:500	Thermo Fisher Scientific A21206	AB_2535792
Anti-rabbit Alexa Fluor 546	Donkey	1:500	Thermo Fisher Scientific A10040	AB_2534016
Anti-rabbit Alexa Fluor 635	Goat	1:500	Thermo Fisher Scientific A31577	AB_2536187
Streptavidin Alexa Fluor 488	–	1:1,000	Thermo Fisher Scientific S32354	AB_2315383

then reacted with 0.375 mg/ml nitroblue tetrazolium and 0.188 mg/ml 5-bromo-4-chloro-3-indolylphosphate (NBT/BCIP; Roche Diagnostics, Basel, Switzerland) for 27–42 h. Sense probes detected no signal higher than the background. To sensitively detect the signals for *Drd1a* and *Drd2* mRNA, we also applied the BT-GO amplification method as aforementioned in section “Tracer visualization.” Briefly, after hybridization with DIG-labeled *Drd1a* and *Drd2* riboprobes, the sections were incubated with 1:4,000 diluted peroxidase-conjugated anti-DIG sheep antibody (11-207-733-910; Roche Diagnostics, Basel, Switzerland). Subsequently, the sections were reacted with a mixture containing 31  $\mu$ M BT, 3  $\mu$ g/ml of GO, 2 mg/ml of beta-D-glucose, and 2% bovine serum albumin in 0.1 M PB for 30 min. The sections were further incubated with 1:1,000 diluted alkaline phosphatase-conjugated streptavidin (02516-71; Nacalai Tesque) for 2 h and finally reacted with NBT/BCIP. The probes for *Drd1a* (target sequence position, 1116-1809 GenBank:

NM\_010076.3, gifted from Dr. Shinichiro Okamoto) and for *Drd2* (target sequence position, 1412–2497 GenBank: X55674.1, gifted from Dr. Shinichiro Okamoto) were used.

After *in situ* hybridization, the sections were processed for NeuN immunohistochemistry for conventional visualization with bright microscopy using avidin-biotin-peroxidase complex (ABC Elite; Vector Laboratories, Burlingame, CA, United States) and diaminobenzidine. The stained sections were serially mounted onto the gelatinized glass slides, dried, washed in running water, dried again, cleared in xylene, and finally covered with mounting medium MX (Matsunami, Kishiwada, Japan) and a glass coverslip. The boundaries of the D1R- and D2R-poor zones were determined with double immunofluorescent staining for D1R and D2R using the adjacent section.

## Electrophysiological Recording and *post hoc* Immunofluorescence

The electrophysiological recording using *in vitro* slice preparation was conducted as previously reported (Karube et al., 2019). Briefly, a mouse (postnatal 3–4 weeks) was deeply anesthetized with isoflurane and decapitated. The brain was removed from the skull and immediately cooled for 2 min in ice-cold artificial cerebrospinal fluid (ACSF) oxidized with 95% O<sub>2</sub>/5% carbon dioxide (CO<sub>2</sub>) gas. Then, a brain block containing the striatum was resected and coronally sectioned into slices of 300  $\mu\text{m}$  thickness using a vibratome (7000smz-2, Campden, Leicestershire, United Kingdom) in cold ACSF. The sections were incubated for 20 min at 32°C and then over 1 h at RT for recovery. Striatal neurons and neurons in the neighboring nuclei were recorded using the whole-cell patch-clamp method with the aid of an EPC10 amplifier (HEKA Elektronik Dr. Schulze GmbH, Lambrecht/Pfalz, Germany). The pipette solution was composed of potassium gluconate 130; KCl; Na<sub>2</sub>ATP 3; Na<sub>3</sub>GTP 0.3; MgCl<sub>2</sub> 2; Na<sub>4</sub>EGTA.6; HEPES 10; biocytin 20.1 (in mM). The pH was adjusted to 7.3 with KOH, and the osmolality was  $\sim$ 290 mOsm. To obtain the relationship between action potential frequency and input current intensity, 1,000 ms of depolarized current pulses were applied with a 50 pA-increment step. From the data, rheobase current was calculated. After electrophysiological recording, an image of the slice and electrode tip was acquired to clarify the location of the recorded neurons in the striatum. The slices were fixed overnight with a fixative composed of 4% paraformaldehyde and 0.2% picric acid dissolved in 0.1 M PB. The fixed slices were re-sectioned into 50  $\mu\text{m}$  slices, and the recorded neurons filled with biocytin were visualized using fluorophore-conjugated streptavidin. D1R, D2R, and DARPP32—a marker of MSNs—were identified by immunofluorescent labeling as described above (see section “Immunofluorescence labeling and tracer visualization”) to confirm the location of the recorded neurons, and to confirm if they were MSNs. The image was aligned to the corresponding image taken at recording to identify individual neurons.

## Image Acquisition and Processing

The specimens were observed using the following microscopes: all-in-one fluorescence microscope (BZ-X710; Keyence, Osaka,

Japan); BX53 (equipped with a DP73 CCD camera; Olympus, Tokyo, Japan) or a confocal microscope (FV1200, Olympus). For fluorescent imaging, appropriate filter sets [359–371-nm excitation and 397-nm emission for Alexa Fluor (AF) 350 or 405; 450–490-nm excitation and 514–565-nm emission for AF488; 530–550-nm excitation and  $>$ 575-nm emission for AF546 or AF555; 590–650-nm excitation and 655–675-nm emission for AF635] were applied. The images of each channel were obtained sequentially and separately to negate the possible crosstalk of signals across channels. Sections processed for *in situ* hybridization were observed with bright field microscopy.

To quantify and compare immunofluorescent signals for D1R, D2R, and tyrosine hydroxylase (TH) across the striatal regions and among individual mice, first D1R- and D2R-poor regions were approximately determined using immunofluorescent images of a sagittal section. A line was drawn to connect the ventral border of the internal capsule (ic) and the mid point of the rostral edge of the D1R-poor zone, then the line was extended toward the cerebral cortex in a linear fashion (Figure 2B). Finally, a pixel intensity profile along the line was obtained. The precise borders between the rostral striatum and D1R-poor zone, D1R-poor zone and D2R-poor zone, or D2R-poor zone and ic, were confirmed using the derivative of each line plot as the point of maximum slope. Finally, regions of interest (ROIs) (200  $\times$  200  $\mu\text{m}^2$  unless otherwise noted) were placed in each region along with the line. To measure the pixel intensity of the ROIs, small areas containing nerve bundles were masked.

For the quantification of anterogradely labeled axon distribution (Figures 6, 7), the acquired confocal images (1  $\mu\text{m}$  of Z-spacing) were analyzed using Fiji—an image processing package (Schindelin et al., 2012). The sections were processed for triple fluorescent labeling for BDA- or PHAL-loaded axons, TH, and NeuN in every 120- $\mu\text{m}$  coronal section. Using the fluorescence of TH, NeuN, and the autofluorescence of thick axon bundles (e.g., cerebral peduncle), the contours of GP and SNpl were delineated. The image containing axons was processed with the “subtract background” function of Fiji to reduce background fluorescence, and then Z projection of the image was obtained. Next, the image was thresholded and binarized. The number of pixels containing axons was counted using the binarized image. In individual mice, the labeled axons were contained in 2–4 GP sections, and 3–5 SNpl sections. Since the number of the axon pixels varied among sections, especially for GP, the maximum number of pixels per section was compared between axons in GP and axons in SNpl.

## Statistical Comparison

All averaged values are represented as mean  $\pm$  SD. The quantitative values among groups ( $>$ 2) were compared using one-way ANOVA followed by the *post hoc* Tukey’s test with the aid of software: Microsoft Excel, R (language and environment for statistical computing and graphics similar to S<sup>1</sup>), and MATLAB (MathWorks, Natick, MA, United States). Comparisons between two data groups were conducted using a

<sup>1</sup><http://cran.r-project.org/>

*t*-test. All *p*-values are presented; *p*-values less than 0.05 were considered to be statistically significant.

## RESULTS

### Uneven Distribution of Immunoreactivity of Dopamine Receptor D1 and Dopamine Receptor D2 in the Mouse Caudal Striatum

In marked contrast to the dorsal, rostral, or medial striatum, D1R-immunoreactivity was weak from 1.1 to 2.0 mm posterior to the bregma (AP  $-1.1$  –  $-2.0$ ) and from 2.7 mm to 3.3 mm lateral to the midline (L 2.8 – 3.3), whereas D2R-immunoreactivity was weak in the range of AP  $-1.2$  –  $-1.8$  and L 2.7 – 3.2 in mice. Representative immunofluorescent images for D1R, D2R, and TH on sagittal and coronal planes of the striatum are shown in **Figure 1**. Uneven distributions of D1R, D2R, and TH were obviously observed in the caudal (AP  $-1.3$ ,  $-1.6$ , and  $-1.9$  in coronal plane in **Figure 1A**) and lateral (L 2.9, 3.0, 3.2, and 3.3 in sagittal plane in **Figure 1B**) part of the striatum. The zone with weak D1R and that with weak D2R separately existed (arrowhead in **Figure 2A**; cf. Gangarossa et al., 2013b; Miyamoto et al., 2019). Hereafter, they are referred to as D1R-poor zone and D2R-poor zone, respectively. In these zones, immunofluorescence for TH was also weak (**Figures 1, 2A**; Miyamoto et al., 2019). A representative sagittal section (L3.0) and the definition of the striatal area used in this study are shown in **Figure 2A**, respectively. This characteristic spatial expression of D1R, D2R, and TH was always observed in all samples used for this study ( $N = 45$  mice). To quantify these changes of fluorescence, fluorescence intensity line profiles were obtained for D1R, D2R, and TH as shown in **Figure 2B** ( $N = 3$  mice; one section/mouse; see Materials and Methods in section “Image acquisition and processing”). The fluorescence intensity was compared in ROIs located at the rostral striatum (rStr), D1R-poor zone, and D2R-poor zone, and then normalized by the values of rStr (**Figure 2C**). Normalized D1R pixel intensity was significantly different among the zones as analyzed by one-way ANOVA ( $F = 104.25$ ,  $p = 2.2 \times 10^{-5}$ ). D1R expression was lower in D1R-poor zone ( $0.53 \pm 0.02$ ) than rStr ( $P = 0.00002$ ) or D2R-poor zone ( $0.92 \pm 0.06$ ;  $P = 0.00008$ ) with *post hoc* Tukey’s test. D2R was also expressed differentially among zones ( $F = 131.44$ ,  $P = 1.1 \times 10^{-5}$  by one-way ANOVA). In contrast to D1R, D2R expression was significantly lower in D2R-poor zone ( $0.33 \pm 0.08$ ) than rStr ( $P = 0.00003$  with *post hoc* Tukey’s test) or D1R-poor zone ( $1.09 \pm 0.03$ ;  $P = 0.00001$ ). In addition, TH expression differed among zones ( $F = 336.89$ ,  $p = 6.9 \times 10^{-7}$  by one-way ANOVA). The pixel intensity was lower in D1R-poor zones and D2R-poor zone ( $0.41 \pm 0.04$  and  $0.44 \pm 0.03$ , respectively) than rStr ( $P = 0.000001$  for D1R-poor zone and  $p = 0.000002$  for D2R-poor zone). On the other hand, DARPP32, a well-known marker of MSNs, was expressed in the whole area of the striatum including the poor zones (**Figure 2D**). At higher magnifications, the immunofluorescence of DARPP32 in cell bodies was almost similar throughout the striatum (**Figure 2E**),

although it was apparently weak in cStr at low magnification (**Figure 2D**). When combined with NeuN-immunostaining, the number of DARPP32-expressing neurons was counted in ROIs placed in four striatal subregions (ROI size,  $318 \times 318 \mu\text{m}^2$ ; **Figures 2D,E**;  $N = 3$  mice, one section/mouse). The proportion of DARPP32-expressing cells to the number of NeuN-positive cells was  $94.3 \pm 1.3\%$  in rStr ( $N = 437/464$  NeuN-expressing cells),  $93.5 \pm 0.9\%$  in para-poor zones (ppz,  $N = 392/419$ ),  $92.6 \pm 0.5\%$  in D1R-poor zones ( $N = 465/502$ ), and  $92.1 \pm 0.5\%$  in D2R-poor zones ( $N = 396/430$ ) (**Figure 2F**). The proportion was not significantly different among rStr, para-poor zones, and two poor zones ( $F = 2.95$ ,  $p = 0.15$ , analyzed by one-way ANOVA).

Dopamine transporter (DAT) is purely expressed in the dopaminergic nervous system, while TH is expressed in catecholaminergic axons as well as dopaminergic axons. Thus, we examined whether DAT expression showed a similar spatial pattern to TH. As shown in **Supplementary Figure 1**, distributions of DAT and TH highly overlapped in the whole striatum, except for subcallosal zones where TH expression was relatively low. The line profile for DAT immunofluorescence correlated highly with that for TH (**Supplementary Figure 1B**, Pearson’s correlation coefficient was  $0.953 \pm 0.012$ ,  $p < 2.2 \times 10^{-6}$ ;  $N = 3$  mice, one section/mouse). DAT immunofluorescence was significantly lower in the caudoventral striatum (cvStr) than rStr (**Supplementary Figure 1C**;  $p = 0.03125$ ;  $N = 2$  ROIs for each rStr and cvStr in each section;  $N = 3$  mice; one section/mouse). Normalized intensity in cvStr was  $0.475 \pm 0.111$  for DAT and  $0.457 \pm 0.114$  for TH.

### Uneven Distribution of Messenger RNA of Dopamine Receptor D1 and Dopamine Receptor D2 in Caudal Striatal Neurons in Mice

Since D1R and D2R are also expressed in presynaptic terminals, it is not clear whether the above investigation reflects differential cellular compositions of specific areas of the cStr. Even if the fluorescence mainly came from cell bodies, different fluorescence intensities could reflect total neuronal density among striatal regions. To directly solve the question, we investigated the messenger RNA (mRNA) expression of *Drd1a* and *Drd2* genes by *in situ* hybridization. A section containing the poor zones was used for *in situ* hybridization with NeuN immunostaining. To confirm the poor zone identity, the adjacent section was used for the double immunofluorescent staining of D1R and D2R (**Figures 3A,B,D,E**). *Drd1a* (**Figures 3A,B**) and *Drd2* (**Figures 3D,E**) were detected (dark blue) in cell bodies of striatal neurons expressing NeuN (brown). To compare zonal differences in the number and proportion of D1R- or D2R-neurons, we counted them in four areas: rStr, para-poor zone, D1R-poor zone, and D2R-poor zone (as shown in **Figure 2A** for subdivision of the striatum used in this study). The number of NeuN immunopositive cells did not significantly differ among four ROIs ( $N = 3$  mice; one section/mouse;  $N = 5,689$  neurons in total;  $F = 1.26$ ,  $p = 0.14$  by one-way ANOVA; **Figure 3G**), suggesting that the cell density of the striatum, most of which is probably regarded as the MSNs density (**Figure 2F**), seems to

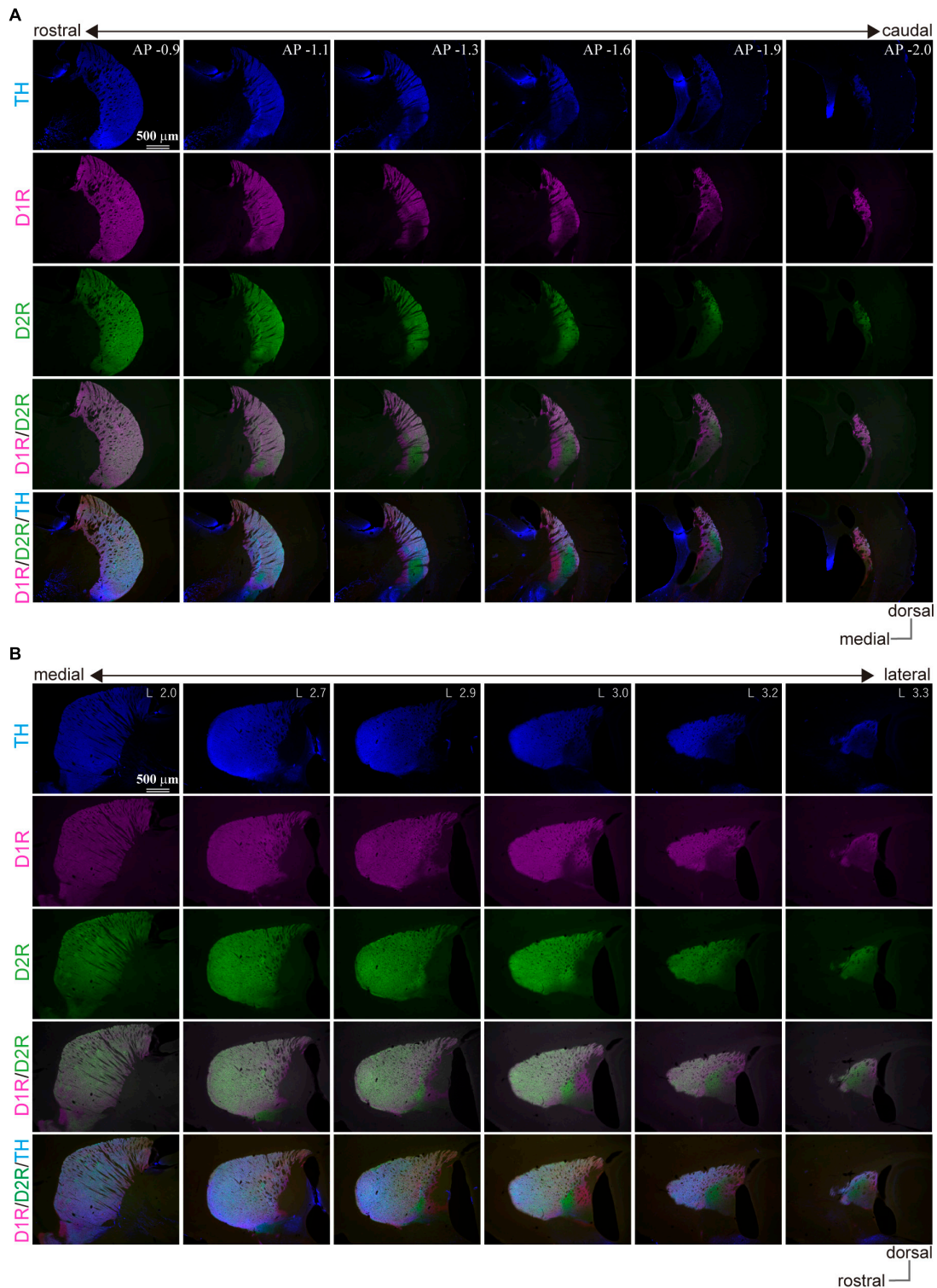


**FIGURE 1** | Uneven distribution of immunofluorescence for dopamine receptor D1 (D1R), dopamine receptor D2 (D2R), and tyrosine hydroxylase (TH) in the mouse caudal striatum. Images of immunofluorescent labeling against TH (blue), D1R (magenta), and D2R (green) show the explicit location of the D1R/D2R-poor zones in the mouse striatum. **(A)** Coronal plane. The number seen after the abbreviation “AP” at the right upper corner of the top-row images represents “distance from the bregma” in mm. **(B)** Sagittal plane. The number seen after the abbreviation “L” at the right upper corner of the top-row images represents “lateral distance from the midline” in mm.

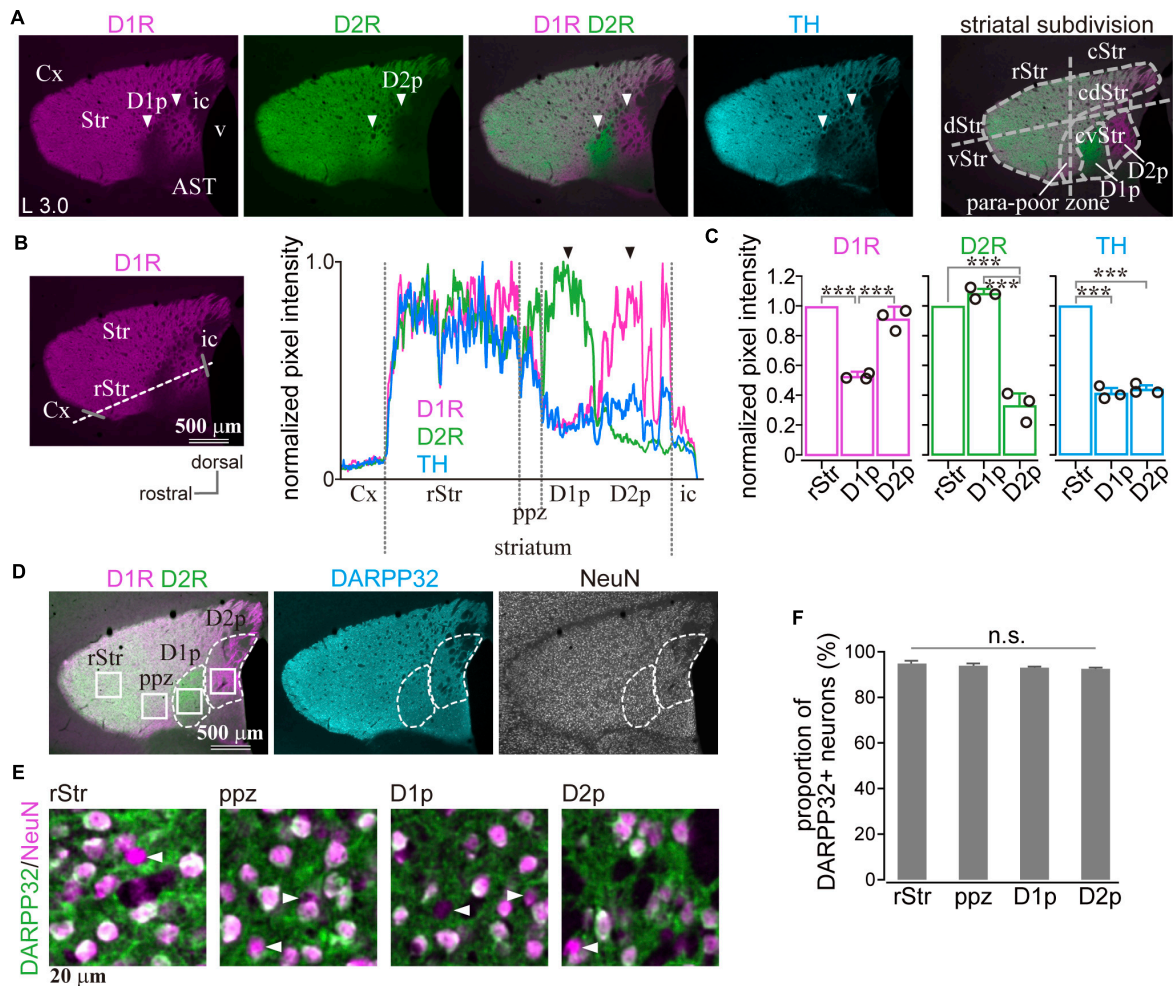


**FIGURE 2** | Quantification of dopamine receptor D1 (D1R), dopamine receptor D2 (D2R), and tyrosine hydroxylase (TH) expression in the caudal striatum. **(A)** Images of immunofluorescent labeling for D1R (magenta), D2R (green), and TH (cyan) of the mouse striatum. Arrowheads indicate the regions with a very faint signal as either D1R or D2R. For this paper, the lateral striatum is subdivided into the rostral (rStr) and caudal striatum (cStr); the dorsal (dStr) and ventral striatum (vStr); cStr is further divided into the caudo-dorsal (cdStr) and caudoventral striatum (cvStr), as shown in the rightmost panel. D1R- and D2R-poor zones (abbreviated as D1p and D2p, respectively) were situated in cvStr. The region surrounding the poor zones is named here as the para-poor zone in which a nearly uniform expression of D1R and D2R is seen. **(B)** Quantification of pixel intensity along a dotted white line. Gray bars represent the rostral and caudal edges of the striatum. The right panel shows normalized pixel intensity in a section of a mouse (3.0 mm lateral from the midline). **(C)** Average pixel intensity ( $N = 3$  mice). Circles indicate individual data. **(D)** Quadruple immunostaining against D1R, D2R, NeuN, and DARPP32. DARPP32 was expressed in the whole striatum (cyan). **(E)** Magnified images of NeuN (magenta) and DARPP32 (green) immunostaining. To clearly represent the overlay of NeuN and DARPP32, the pseudocolors were different from those shown in **(D)**. Arrowheads indicate neurons without DARPP32 expression. **(F)** The proportion of DARPP32 expressing neurons. AST, amygdala striatal transition area; Cx, cerebral cortex; ic, internal capsule; v, ventricle.  $***P < 0.001$ . not significant (n.s.).

be uniform even in the two poor-zones. The number of Drd1a or Drd2 expressing neurons were counted in one representative section for each mouse ( $N = 3$  mice; one section/mouse;  $N = 2,615$  neurons for Drd1a and  $N = 3,074$  neurons for Drd2). The proportion of Drd1a-expressing neurons to total neurons was  $12.23 \pm 1.43\%$  ( $N = 73/593$  neurons as sum of three mice) in D1R-poor zones,  $82.06 \pm 3.08\%$  ( $N = 528/645$ ) in D2R-poor zones,  $50.44 \pm 0.07\%$  ( $N = 354/702$ ) in rStr, and  $46.49 \pm 1.34\%$  ( $N = 315/675$ ) in para-poor zones, which were significantly different among these regions ( $F = 579.5$ ;  $P = 0.0000507$  using one-way ANOVA). *Post hoc* Tukey's test

revealed that the proportion of Drd1a-expressing neurons was significantly lower in D1R-poor zones ( $P = 0.0000001$  vs. rStr;  $P = 0.0000001$  vs. para-poor zone;  $P = 0.0000001$  vs. D2R-poor zone), and significantly higher in the D2R-poor zone than the other three regions ( $P = 0.0000001$  vs. rStr;  $P = 0.0000001$  vs. para-poor zone) (**Figure 3C**). No significant difference was observed for rStr vs. para-poor zone ( $P = 0.13$ ). Contrastingly, the proportion of Drd2-expressing neurons to total neurons was  $78.68 \pm 1.73\%$  ( $N = 539/686$ ) in D1R-poor zone,  $3.58 \pm 1.19\%$  ( $N = 28/786$ ) in D2R-poor zone,  $46.78 \pm 4.23\%$  ( $N = 366/781$ ) in rStr, and  $46.73 \pm 4.13\%$  ( $N = 382/821$ ) in the para-poor

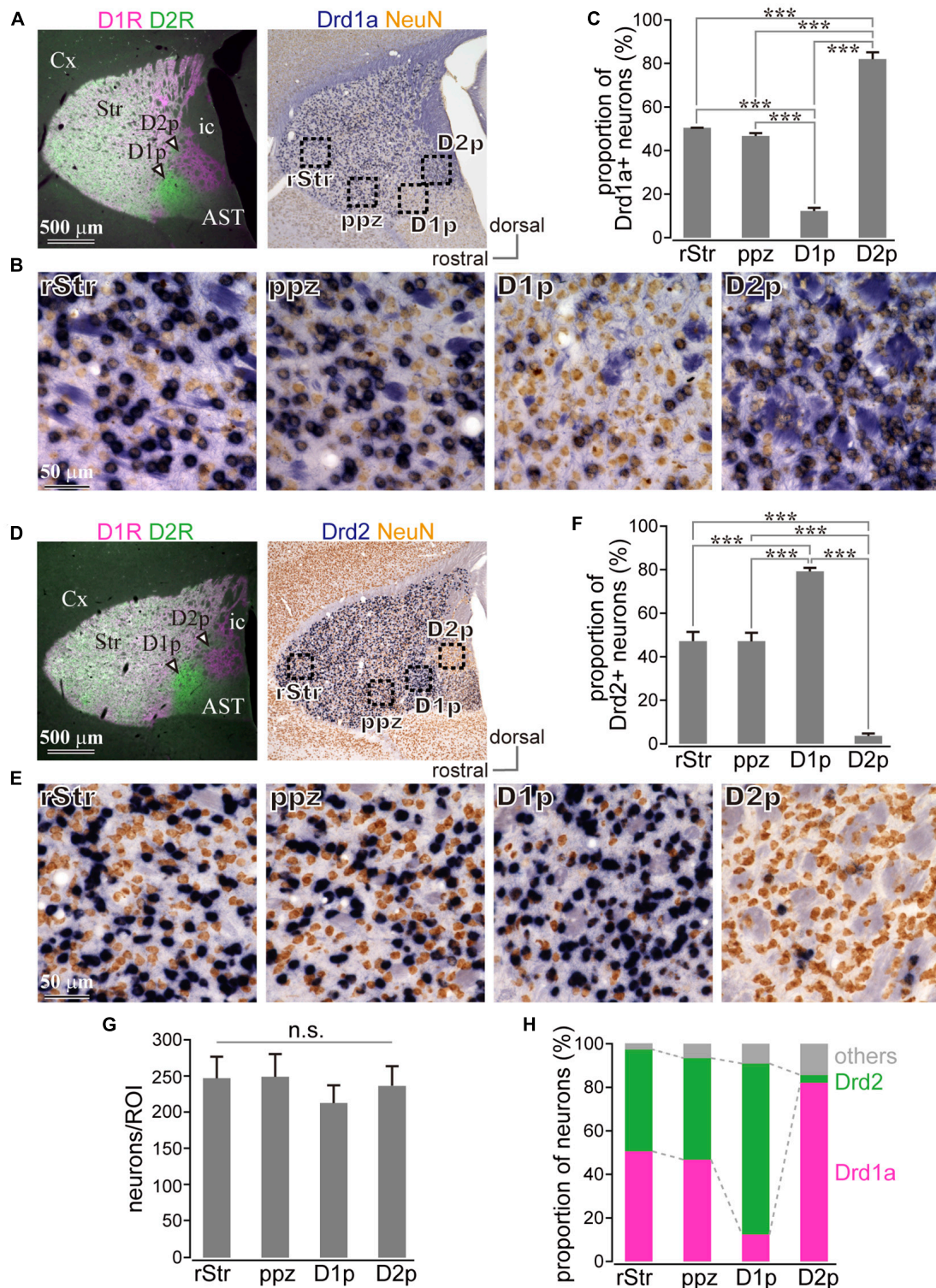


**FIGURE 3 |** Uneven distribution of D1R or D2R messenger RNA (mRNA) expressing neurons in the caudal striatum. **(A,D)** Left, Images of immunofluorescent labeling for D1R (magenta) and D2R (green). Right, Drd1a- **(A)** or Drd2- **(D)** expressing neurons (blue) with immunostaining against NeuN (brown). **(B,E)** Magnified images of rectangle areas 1–4 in **(A)** or **(D)**. **(C,F)** Proportion of Drd1a- or Drd2-expressing neurons in rostral (rStr), para-poor zone (ppz), D1R-poor zone (D1p) or D2R-poor zone (D2p) ( $N = 3$  mice for each). **(G)** Mean NeuN+ cell number in each region of interest (ROI). **(H)** Elucidated cell composition in each striatal area. AST, amygdala striatal transition area; Cx, cerebral cortex; ic, internal capsule; v, ventricle.  $***P < 0.001$ . not significant (n.s.).

zone. The proportion was significantly different among these four regions ( $F = 998.48$ ;  $P = 0.00000276$  using one-way ANOVA). D2R-poor zone contained a significantly lower proportion of D2R-expressing neurons than the other regions ( $P = 0.0000007$  vs. rStr;  $P = 0.0000007$  vs. para-poor zone;  $P = 0.0000001$  vs. D1R-poor zone). The D1R-poor zone contained a significantly higher number of D2R-expressing neurons than others ( $P = 0.0000076$  vs. rStr;  $P = 0.0000075$  vs. para-poor zone) (Figure 3F). Again, no significant difference was observed between rStr and the para-poor zone ( $P = 0.99$ ). Since we could not visualize both Drd1a and Drd2 simultaneously, their composition in each area was elucidated as the sum of individual data in Figure 3H. These results clearly indicate the distinct cell type composition of both D1R- and D2R-poor zones, in which either D2R or D1R expressing neurons occupied approximately 80% of total neurons. In the D2R-poor zone, the proportion of neurons expressing neither D1R nor D2R was slightly larger than in other zones. We also compared interneuron density for neurons expressing parvalbumin, calretinin, or choline acetyl transferase. As Miyamoto et al. (2019) reported, subtle differences were observed. However, this information is still insufficient to explain the proportion of neurons that lack D1R/D2R expression in the D2R-poor zone.

### Medium Spiny Neurons in Dopamine Receptor D1- or Dopamine Receptor D2-Poor Zones Possessed Similar Membrane Properties to Those in the Dorsal Striatum

Since the poor zones are located close to the boundary between the striatum and the amygdala-striatal transition area (AST) or GP, we wondered whether these dopamine-receptor-expressing neurons are MSNs possessing similar properties to other parts of the striatum. Whole-cell patch-clamp recordings were accomplished from medium-sized neurons in those areas ( $N = 8$  mice), and the recorded neurons were filled with biocytin. The recorded slices were examined for *post hoc* immunofluorescence against D1R, D2R, and DARPP32 (Figures 4A,B). As a result, we obtained medium-sized neurons recorded in the cdStr ( $N = 6$ ) and D1R- ( $N = 5$ ) or D2R-poor zone ( $N = 3$ ) (Figure 4D). They represented similar membrane properties, such as deep resting membrane potentials, narrow action potentials, and low input resistances ( $P > 0.05$  analyzed by one-way ANOVA; Figures 4C,E,F and Table 3). F-I curves, the relationship between action potential frequency and input current intensity, were plotted in Figure 4E. Once action potentials were elicited, the frequency increased linearly during the following 200–300 pA increments of input current. This part of the F-I curve could be linearly fitted well for all neurons ( $r^2 = 0.971 \pm 0.024$ ). The slopes of the fitted lines were not significantly different among the recorded neurons in the three zones (Table 3,  $F = 1.49$ ,  $p = 0.316$  analyzed by one-way ANOVA). A significant difference was observed for rheobase current in the cdStr, D1R- and D2R-poor zones ( $F = 6.74$ ,  $p = 0.012$  by one-way ANOVA; Figure 4F). *Post hoc* Tukey's test indicated that the rheobase current of the neurons was lower in the D1R-poor zone than in cdStr

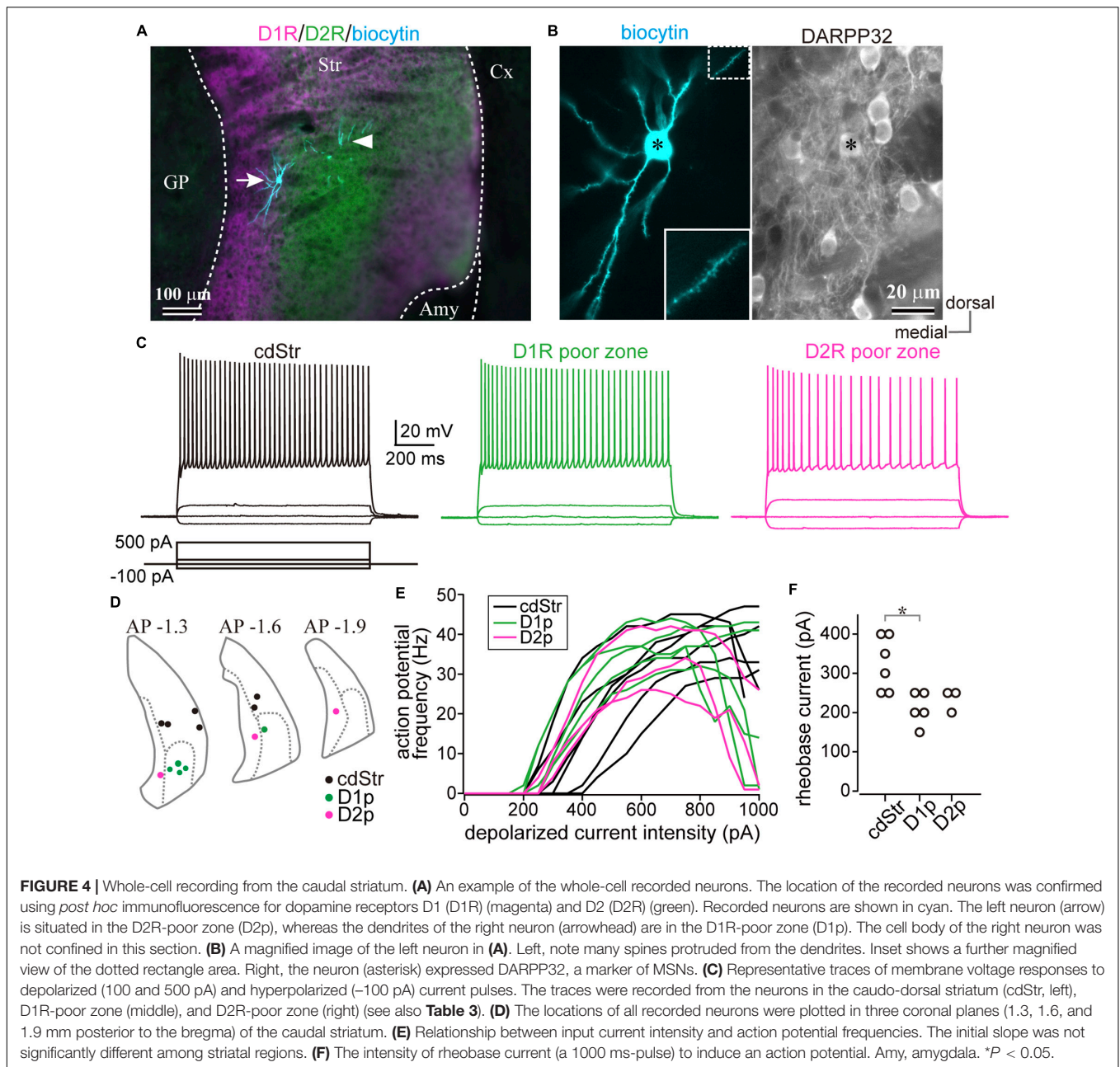
( $P = 0.013$ ). The threshold of an action potential (elicited by a brief pulse of 10 ms) was not significantly different among the three zones ( $F = 0.49$ ,  $P = 0.627$  by one-way ANOVA). In addition, all neurons which could be examined were positive for immunofluorescence against DARPP32 ( $N = 3/3$  neurons in the cdStr,  $N = 5/5$  in D1R-poor zone, and  $N = 3/3$  in D2R-poor zone). The cell bodies of the remaining 3/6 cdStr recorded neurons were not recovered; therefore they could not be examined for DARPP32 expression. In some neurons, their dendrites were well visualized, and they were spiny (Figure 4B inset). Thus, both poor zones are composed of MSNs, similar to the cdStr.

### Retrogradely Labeled Direct Pathway Neurons Were Abundantly Distributed in the Dopamine Receptor D2-Poor Zone in the Mouse Caudal Striatum

To explore whether D1R-expressing neurons in the poor zones project to the output nuclei of the basal ganglia, i.e., the direct pathway neurons, retrograde neural tracing was conducted. To compare the proportion of retrogradely labeled neurons among striatal regions including rStr and cStr, the tracer injection should have enough volume to efficiently label the neurons regardless of their topographic projections. Therefore, a large volume of CTB555 or CTB488 was injected in wide brain regions located along the striatonigral pathway. It is crucial that the injection must be located posterior to GP, to avoid labeling of the indirect pathway neurons. As shown in Figure 5A, the tracer injection extended to the SNpr, SNpc, and EP, but not to GP. As virtually all direct pathway neurons possess axon collaterals in GP in rodents (Kawaguchi et al., 1990; Wu et al., 2000; Fujiyama et al., 2011), we did not attempt to visualize the indirect pathway neurons in the same way.

The retrogradely labeled neurons were abundantly distributed in the whole striatum with the exception of fewer neurons in D1R-poor zone (Figure 5B). For quantification, an ROI ( $318 \times 318 \mu\text{m}^2$ ) was sampled from each striatal region: rStr (Figure 5C1), para-poor zone (Figure 5C2), D1R-poor zone (Figure 5C3), and D2R-poor zone (Figure 5C4) ( $N = 3$  mice; one section/mouse). In total, 2,252 retrogradely labeled neurons, which can be considered as the direct pathway neurons, were counted stereologically. The density of labeled neurons in the four striatal regions was significantly different ( $F = 62.392$ ;  $P = 0.00068$  using one-way ANOVA). The density was lower in the D1R-poor zone ( $2.57 \pm 0.42 \times 10^4$  neurons/ $\text{mm}^3$ ) than rStr ( $7.52 \pm 0.50 \times 10^4$  neurons/ $\text{mm}^3$ ,  $P = 0.0018$  using *post hoc* Tukey's test), para-poor zone ( $8.30 \pm 1.12 \times 10^4$  neurons/ $\text{mm}^3$ ,  $P = 0.00068$ ), or the D2R-poor zone ( $11.32 \pm 1.63 \times 10^4$  neurons/ $\text{mm}^3$ ,  $P = 0.00003$ ) (Figure 5D). In contrast, the density of labeled neurons in the D2R-poor zone was significantly higher than rStr ( $P = 0.009$ ), the D1R-poor zone, and para-poor zone ( $P = 0.03$ ) (Figure 5D). These results were consistent with the mRNA expression in the poor zone neurons.

In addition, to confirm that the retrogradely labeled neurons expressed D1R, we also combined *in situ* hybridization with retrograde tracing study for bright field microscopy using immunoreaction against CTB ( $N = 1$  mouse, two sections). As



shown in **Figures 5E,F**, CTB labeled neurons (brown), regarded as direct pathway neurons, expressed *Drd1a* (99.3%,  $N = 863/869$ ) but not *Drd2* (1.1%,  $N = 9/843$ ) mRNA (blue).

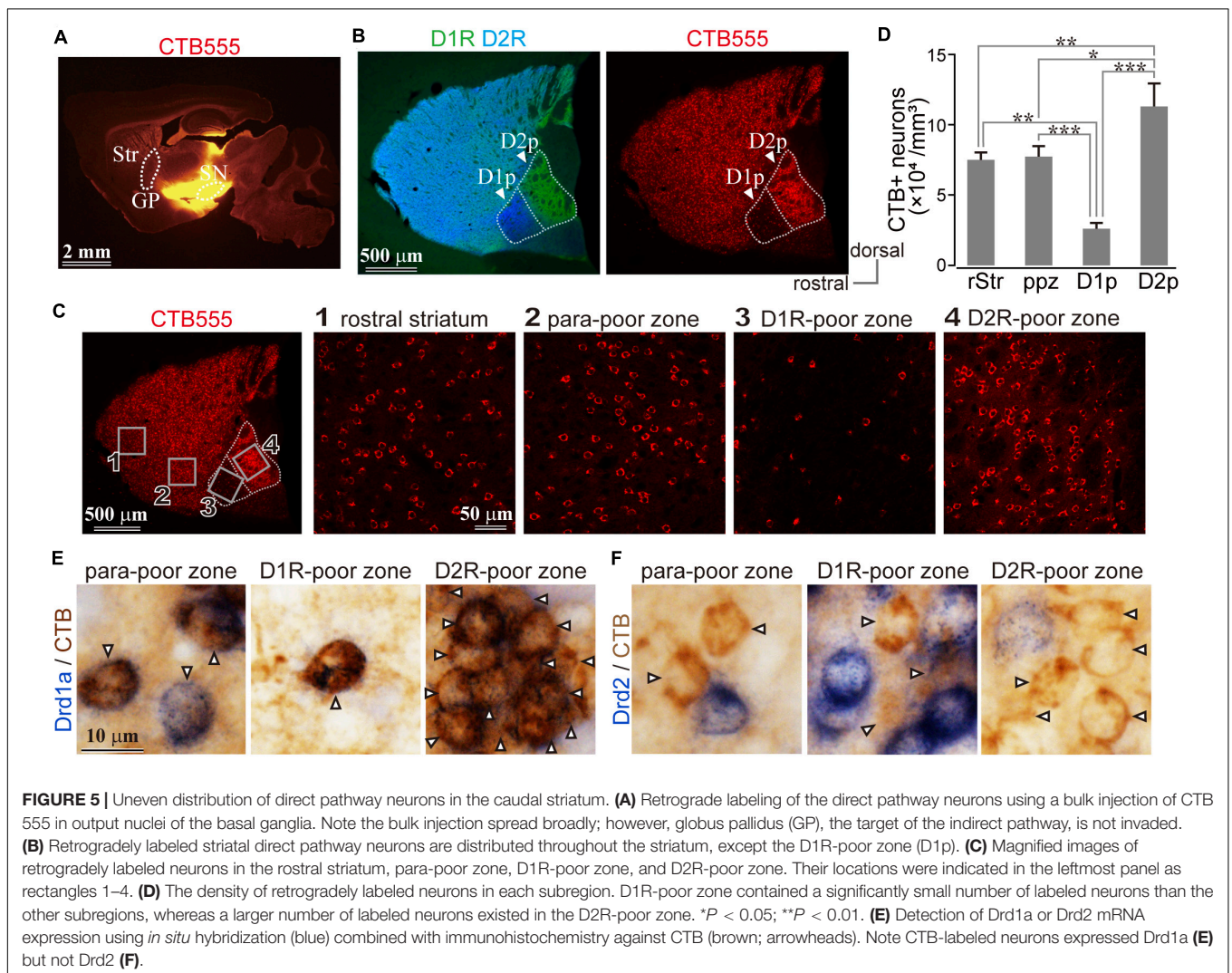
### Axonal Projections From Caudo-Dorsal Striatum, Dopamine Receptor D1- or Dopamine Receptor D2-Poor Zones in Mouse

So far, we have shown that the D1R-poor zone is composed of 79% of indirect pathway neurons expressing D2R, whereas the D2R-poor zone is composed of 82% of direct pathway neurons expressing D1R. A crucial question to be uncovered is whether

outputs of D1R- and D2R-poor zones are similar to those of MSNs located in non-poor zones. To visualize their axonal projections, the small volume of anterograde tracer (BDA, 10 kD, or PHAL) was injected into the cStr, including the D1R- and D2R-poor zones. Due to the small extent of the poor zones, the deposit of BDA should be extremely small to avoid spreading the tracer to neighboring striatal regions (**Figures 6A, 7A–D**). Using immunofluorescence for D1R and D2R, the locations of injection sites were examined. Consequently, we obtained four cases of injection to the D1R-poor zone (**Figures 6A1, 7B**) and one case of injection to the D2R-poor zone (**Figure 7D**). In one remaining case, the injection was centered at the border between D1R- and D2R-poor zones (**Figure 7C**). Therefore, the projection

**TABLE 3** | Electrophysiological properties of medium sized neurons in the dorsal striatum, D1R or D2R poor zones.

	Caudo-dorsal striatum	D1R-poor zone	D2R-poor zone	One-way-ANOVA
Resting membrane potential (mV)	$-81.1 \pm 2.4$	$-78.1 \pm 3.0$	$-78.6 \pm 4.18$	$F = 1.78$ $p = 0.26$
Input resistance (M $\Omega$ )	$52.7 \pm 8.6$	$77.4 \pm 20.0$	$85.3 \pm 36.4$	$F = 4.11$ $p = 0.10$
Time constant (ms)	$4.33 \pm 1.7$	$6.0 \pm 2.1$	$6.7 \pm 1.94$	$F = 1.87$ $p = 0.24$
Action potential width (ms)	$1.57 \pm 0.1$	$1.60 \pm 0.44$	$1.56 \pm 0.25$	$F = 0.011$ $p = 0.99$
Max action potential frequency (Hz)	$25.0 \pm 13.2$	$34.2 \pm 11.4$	$34.0 \pm 8.0$	$F = 1.08$ $p = 0.40$
Slope of f-I curve ( $\times 10^3$ )	$6.42 \pm 4.15$	$9.57 \pm 4.79$	$6.45 \pm 3.22$	$F = 1.49$ $p = 0.316$
Rheobase current (pA)	$325 \pm 69$	$250 \pm 42$	$233 \pm 29$	$F = 6.74$ $p = 0.012$
Action potential threshold (mV)	$-41.12 \pm 2.67$	$-39.64 \pm 5.36$	$-38.61 \pm 2.23$	$F = 1.49$ $p = 0.316$
Number of neurons	6	5	3	



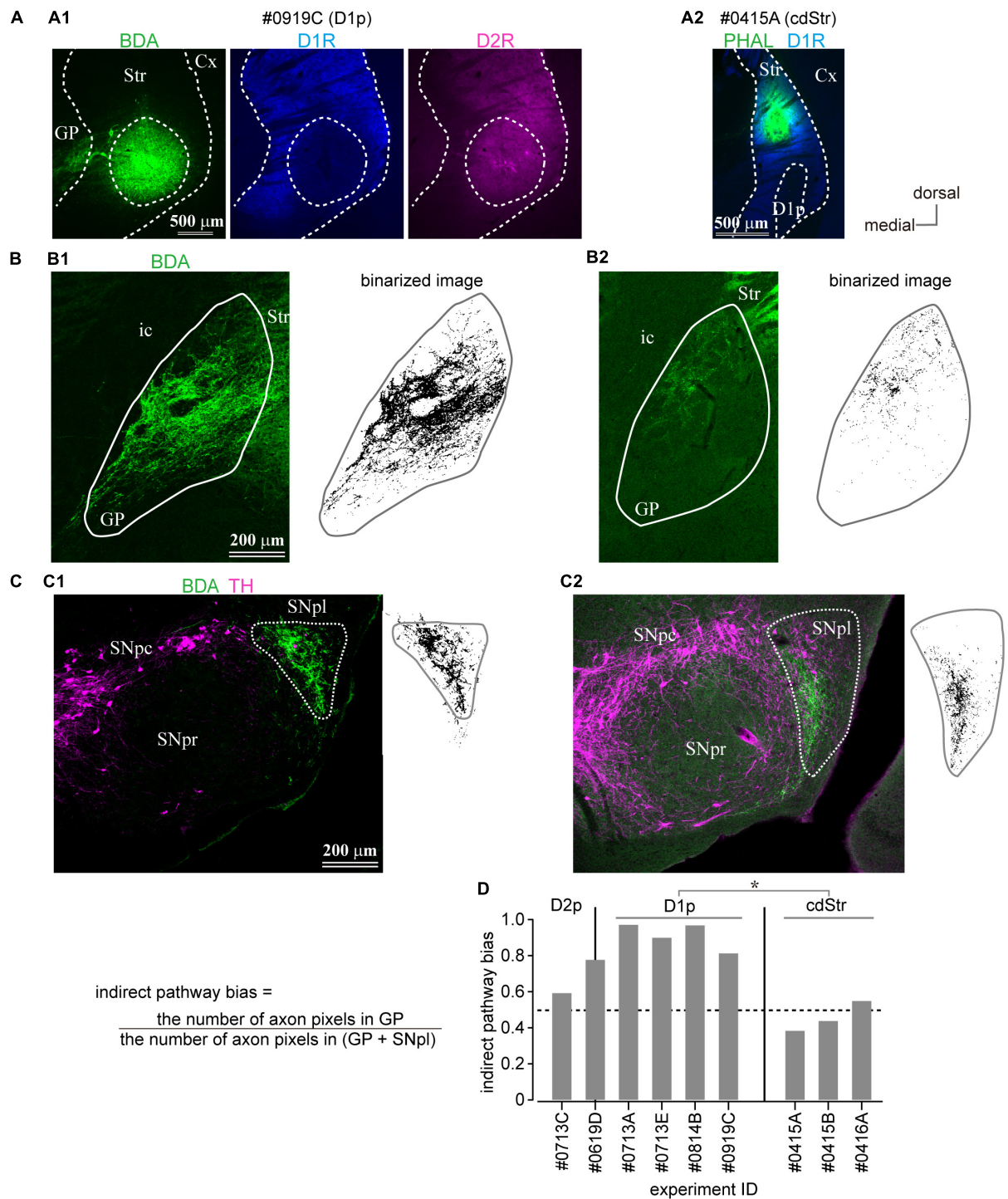


**FIGURE 6 |** Anterograde axon tracing of the caudal striatum. **(A)** Representative examples of tracer injection into the D1R-poor zone **(A1)** or the dorsal part of the caudal striatum (cdStr) **(A2)**. Biotinylated dextran amine (BDA; green) was injected in the D1R-poor zone, whereas Phaseolus Vulgaris Leucoagglutinin (PHAL; green) was injected to cdStr. **(B)** Photoimages (left) and their binarized plots (right) of labeled axons in GP from D1R-poor zone **(B1)** or from cdStr **(B2)**. The binarized pixel plots were used for quantification. **(C)** Photoimages (left) and their binarized plots (right) of labeled axons in substantia nigra (SN) from D1R-poor zone **(C1)** or from cdStr **(C2)**. Note dense axons were highly restricted in substantia nigra pars lateralis (SNpl). Only a few axons in substantia nigra pars reticulata (SNpr) or substantia nigra pars compacta (SNpc). **(D)** Indirect pathway bias (see the main text) of each injection. Injection into the D1R-poor zone resulted in significantly higher values than that into cdStr. Cx, cerebral cortex; GP, globus pallidus; ic, internal capsule; Str, striatum; SNpc, substantia nigra pars compacta; SNpl, substantia nigra pars lateralis; SNpr, substantia nigra pars reticulata. \* $P < 0.05$ .

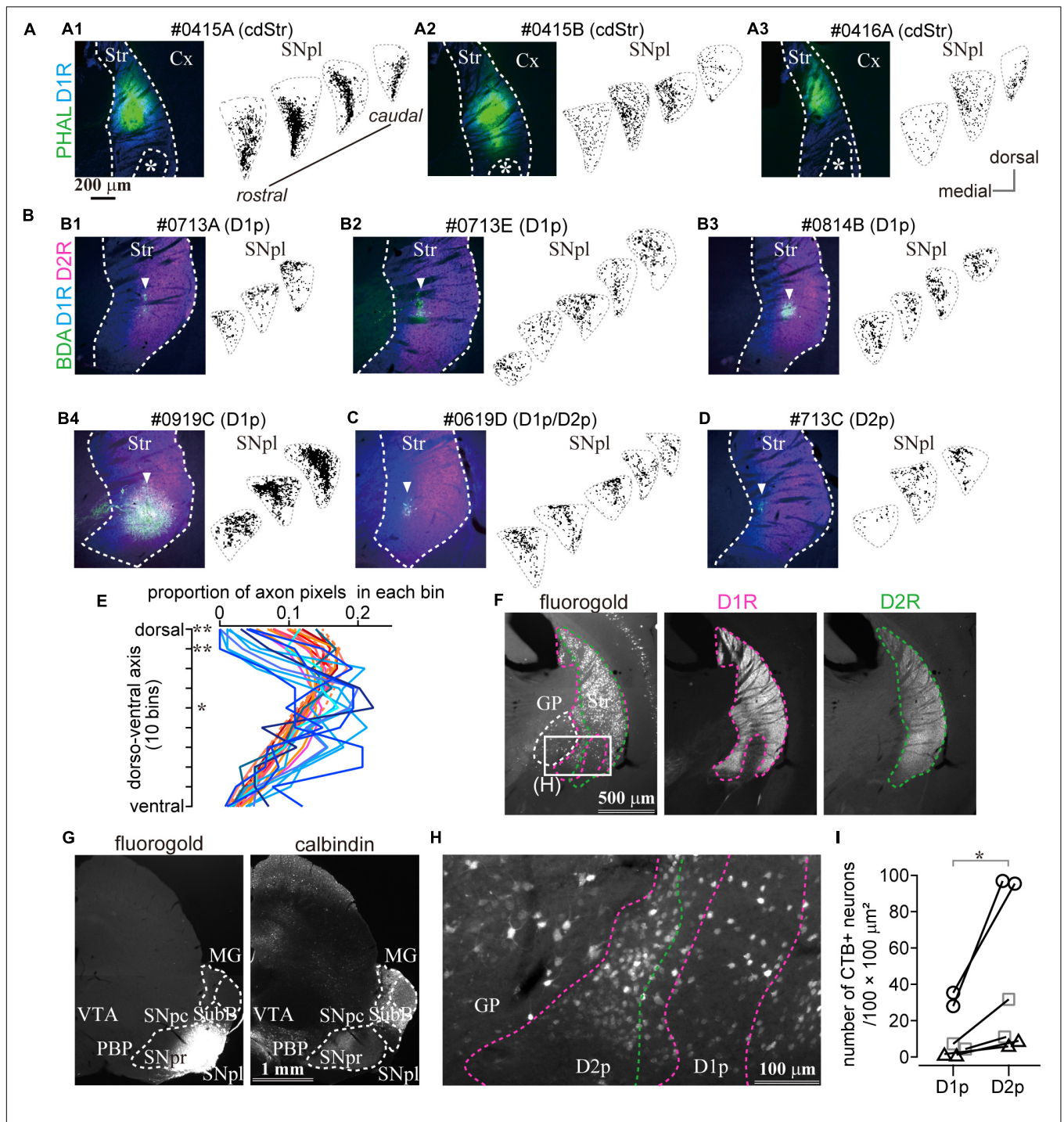


**FIGURE 7 |** The caudal striatum projects to SNpl. **(A–D)** Anterograde tracer injection sites in the caudal striatum (left) and the binarized axon plots in SNpl (right) for all samples. SNpl drawings are arranged in a rostrocaudal order. **(A)** Injections into cdStr ( $N = 3$  mice). Asterisk indicates D1R-poor zone. **(B)** Injections into D1R-poor zone (D1p) ( $N = 4$ ). An arrowhead indicates the center of the injection. **(C)** Injection into the border between D1p and D2R-poor zone (D2p) ( $N = 1$ ). **(D)** Injection into D2p ( $N = 1$ ). **(E)** Comparison of axon distribution in SNpl along a dorso-ventral axis. In the dorsal part of SNpl, axons of the D1R-poor zone (reddish lines) were relatively dense than those of cdStr (bluish lines).  $*P < 0.05$ ;  $**P < 0.01$ . **(F–I)** Retrograde tracer injection into SNpl labeled cStr neurons. **(F)** Left, Neurons labeled by fluorogold injected into SNpl. Immunostaining for D1R (middle) and D2R (right) is used to determine the poor zone. **(G)** Fluorogold injection into SNpl (left). The section was counter stained with calbindin-D-28k (right). Fluorogold extended to the lateral part of SNpr. **(H)** A magnified image of the rectangle area in **(F)**. Labeled neurons were located in GP, D1p, and D2p. **(I)** The number of SNpl projecting neurons in D1R- and D2R-poor zone. The larger number of neurons were labeled in the D2R-poor zone. Individual mice were marked with a different symbol ( $N = 3$  mice, two sections/mouse). Cx, cerebral cortex; MG, medial geniculate nucleus; PBP, parabrachial pigmented nucleus; Str, striatum; SNpc, substantia nigra pars compacta; SNpl, substantia nigra pars lateralis; SNpr, substantia nigra pars reticulata; VTA, ventral tegmental area.

profiles from the poor zones reported here were mainly derived from the D1R-poor zone. For cdStr, the size of injection was larger compared to the poor zones as observed on fluorescent labeling (Figures 6A2, 7A;  $N = 3$  mice). For all injections into cStr (cdStr and the poor zones), the labeled axons were mainly found in GP (Figure 6B and Supplementary Figure 2) and SNpl (Figures 6C, 7A–D and Supplementary Figure 3), and probably, they were targets of the indirect and direct pathway MSNs, respectively. Notably, GP and SNpl were prominent targets of the cStr projections, whereas only a few collaterals were observed in EP, SNpr, and SNpc (Supplementary Figures 2, 3). We counted the number of pixels containing the labeled axons in GP and SNpl using the binarized image in every 120- $\mu\text{m}$  of coronal sections (Figures 6B,C, 7A–D). The anteroposterior extent of axons in GP was restricted in the 2–3 sections containing the caudal GP, whereas axons in SNpl were observed in 3–5 sections. As the axons were much more numerous in only one section for GP, we used the maximum number of axon pixels among multiple sections as an index to represent the strength of projection for both GP and SNpl. The indirect pathway bias, which is the ratio of the maximum number of axon pixels in GP to that in the sum of axons in GP and SNpl, was calculated (Figure 6D). Injection into the D1R-poor zone resulted in a larger indirect pathway bias than that caused by injection into cdStr ( $P = 0.031$  by  $t$ -test). Injections into the D2R-poor zone and into the border between D1R- and D2R-poor zone were excluded from the comparison because only one case for each was obtained. It is suggested that the indirect pathway projections to GP were relatively intensive from the D1R-poor zone than from cdStr. In comparison, cdStr axons tended to be distributed in the ventral part of SNpl (Figure 7A), whereas the poor zones tended to project to the dorsal part of SNpl (Figures 7B–D), as reported previously for cdStr and cvStr (Hintiryan et al., 2016; Hunnicutt et al., 2016; Foster et al., 2021). To quantify and compare axon distribution in SNpl along with the dorso-ventral axis, SNpl in each section was divided into 10 equally bins, then the proportion of axon pixels in each bin to total axon pixels in SNpl of the section was calculated and plotted in Figure 7E [reddish lines for D1R-poor zone projections ( $N = 4$  mice, 16 sections) and bluish lines for cdStr projections ( $N = 3$  mice, 11 sections)]. In the first and second bins, which are located at the most dorsal part of SNpl, the proportion was significantly larger for D1R-poor zone projections than cdStr projections ( $P = 0.0025$  for the first bin by  $t$ -test;  $P = 0.0011$  for the second bin). In the middle of SNpl, the proportion of cdStr projection was larger than that of D1R-poor zone projection ( $P = 0.0234$ ). For the projection to GP, the axons of both poor zones and cdStr were distributed in the caudal GP, not in the rostral GP (Supplementary Figure 2).

We also observed the axons in zona incerta, thalamic ventral posterior nucleus (VPM and VPL), thalamic reticular nucleus (Rt), and medial geniculate nucleus (MG). Because in the cStr (including the poor zones), several neural fibers are passing through; BDA can lead to ectopic labeling—other than the injection center, through such fibers or terminals in the striatum. We found a few labeled neurons in multiple cortical areas, thalamus, and brainstem probably due to retrograde transport of

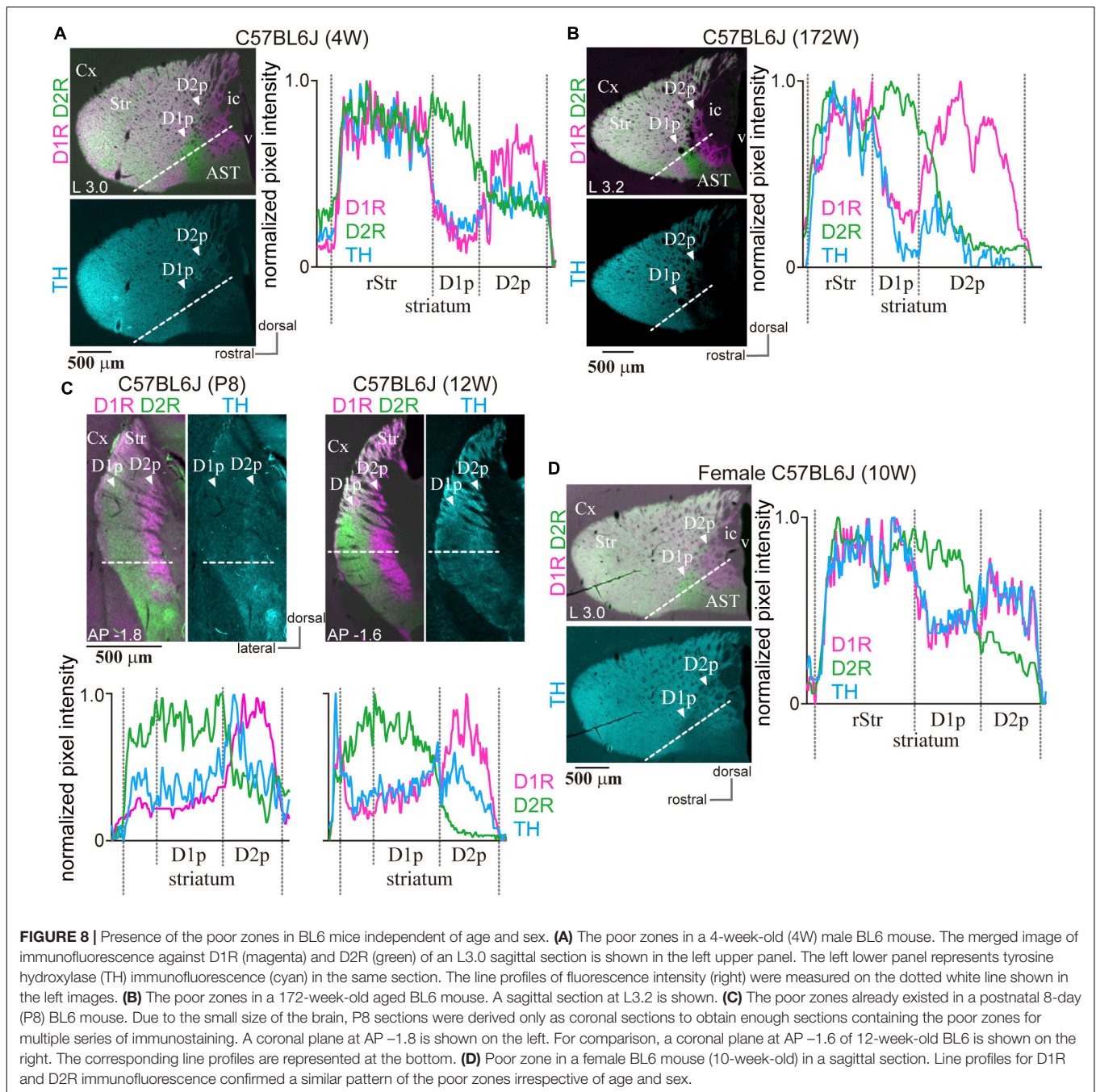
BDA; thus, the above ectopic labeling may be contaminated with actual striatal projections.

To confirm projection from the poor zones, retrograde tracers, fluorogold or CTB555, were injected into either MG or SNpl (Figures 7E,G and Supplementary Figure 4). We found prominent retrograde labeling in cStr including both D1R- and D2R-poor zones by SNpl injection, as well as labeling of large-sized neurons in the caudal GP (Figures 7E,H). The total number of labeled neurons was 249 in the D1R-poor zone and 842 in the D2R-poor zone ( $N = 3$  mice; two sections/mouse). The density of labeled neurons was significantly larger in the D2R-poor zone than in the D1R-poor zone (Figure 7I,  $P = 0.031$  by paired  $t$ -test); this was similar to the case with large volume retrograde tracer injection as shown in Figure 5. On average, the mean ratio of labeled neuron density in the D2R-poor zone vs. that in the D1R-poor zone was  $4.05 \pm 1.74$  (range: 2.51–7.28), reflecting the number of the dMSNs in each zone. This result supported the aforementioned anterograde tracing data which showed that both poor zones projected to SNpl. Meanwhile, little to no labeling in cStr was observed for MG injection; rather MG injection provided intensive labeling in the multiple cortical areas—the primary and secondary somatosensory area (S1 and S2); dorsal and ventral auditory area (Au), temporal association area (TEA), and amygdala. Thus, the main target of the direct pathway in the poor zones must be SNpl (see also Supplementary Figure 4).

### Uneven Distribution of Immunoreactivity of Dopamine Receptor D1 and Dopamine Receptor D2 in the Caudal Striatum Across Age, Sex, Strain, and Species

Since cStr is innervated by the sensory cortices, such as visual and auditory areas, it may be possible that the presence of poor zones depends on intrinsic factors, such as age and sex. Particularly, it is well-known that aged BL6 mice lose their hearing. We examined the poor zones in young (4-week-old;  $N = 3$ ; Figure 8A) and aged ( $N = 3$ ; 61-, 111-, and 172-week-old; Figure 8B) mice. As shown in Figure 8, the poor zones were obviously present irrespective of age. Moreover, even in 8-day-old (P8) mice, the uneven distributions of D1R and D2R were clearly observed (Figure 8C;  $N = 3$  mice). Furthermore, the poor zones were also present in female mice (Figure 8D;  $N = 3$  mice, 10–12-week-old). The line profiles of D1R and D2R immunofluorescence (Figures 8A–D) demonstrated similar spatial distributions to those observed in adult male mice as shown in Figures 1, 2.

To determine whether the uneven distribution of the immunoreactivity of D1R and D2R in cStr is conserved across strains and species, ICR mice (11-week-old,  $N = 3$ ), and Wistar and Long-Evans rats ( $N = 3$  of each; 11–13-week-old) were used to test for triple immunofluorescence of D1R, D2R, and TH. The uneven distribution of D1R and D2R was also found in the cStr of ICR mice (Figure 9A), Wistar rats (Figure 9B), and Long-Evans rats ( $N = 3$ , Figure 9C), as reported for Sprague-Dawley rats previously (Gangarossa et al., 2019). Similar to that of mice, the D2R-poor zone of rats was always located at the most caudal part of the striatum, and the D1R-poor zone was located rostral to and lateral to the D2R-poor zone,



although the appearance of these zones (shape and size) was slightly different than those in mice. The boundary of D1R- and D2R-poor zones extended more dorsally in Long-Evans rats than Wister rats (Figures 9B,C). In addition, the D2R-poor zone spread toward the dorsal edge of the cStr in both strains of rats.

To determine whether the uneven distribution of D1R, D2R, and TH is specific to rodents, the striatum of common marmosets—a non-human primate, was also examined ( $N = 1$  male and 1 female, Figures 9D–F). In primates, the striatum exclusively subdivides further into two nuclei, the putamen, and

caudate nucleus. In the marmoset, the unique region with uneven distribution of D1R and D2R was found around the rostral tip of the tail of the caudate (CDt). D1R- and D2R-poor zones were adjoined, and the D1R-poor zone was located laterally to the D2R-poor zone, as observed in rodents. These uneven distribution zones spread beyond thick nerve bundles (arrows in Figure 9E), which crosses the striatum, and is considered as the border between the putamen and CDt. However, it is difficult to determine whether the spatial composition in the marmosets is similar to that in the rodents owing to anatomical structural differences of the respective striata.

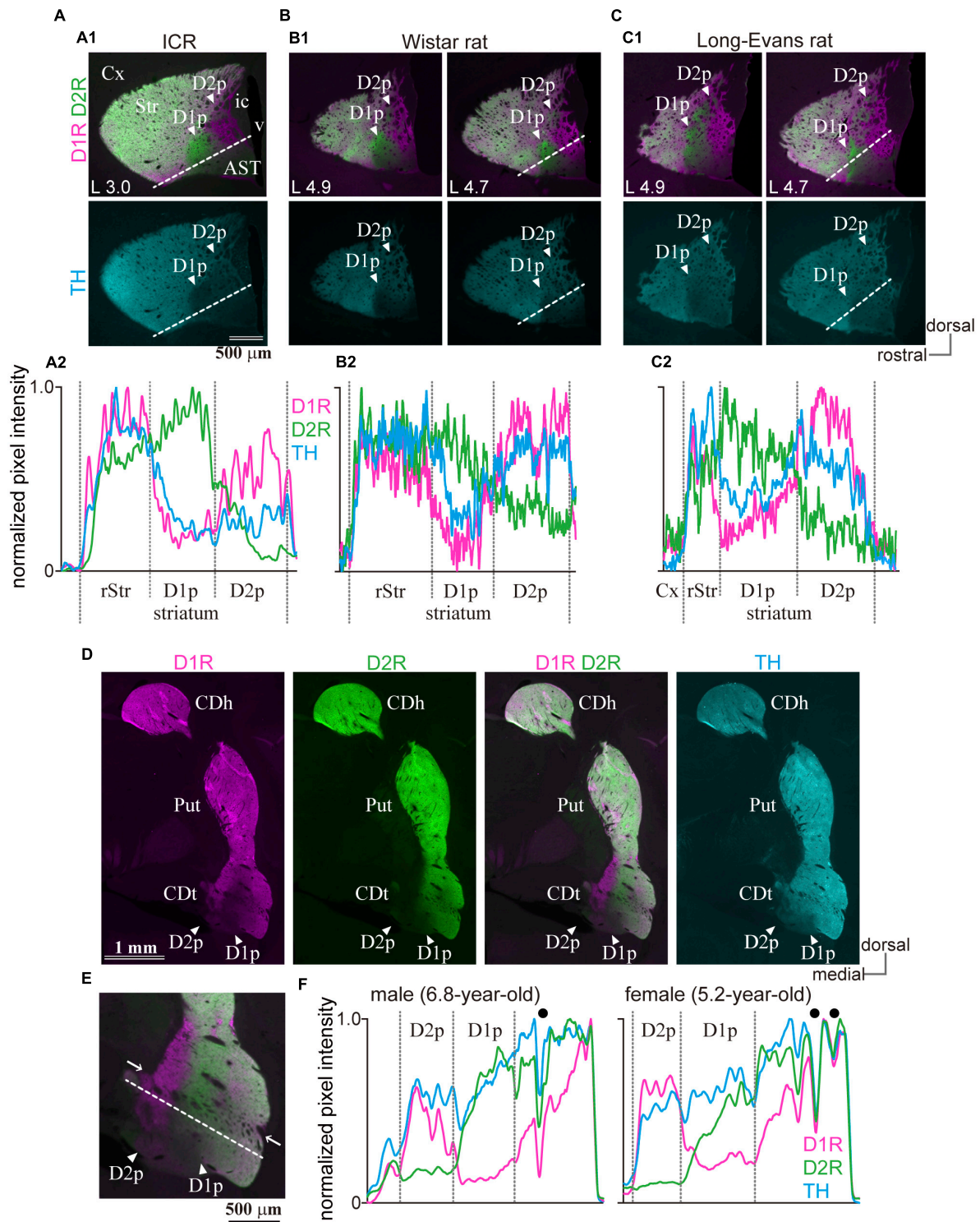


**FIGURE 9** | Presence of the poor zones in ICR mice, rats, and marmosets. **(A1–C1)** Images of immunofluorescent labeling for D1R (magenta), D2R (green), and TH (cyan) in the striatum of rodents. Arrowheads indicate D1R- or D2R-poor zone (D1p or D2p). The distance from the midline is shown at the lower-left corner. **(A2–C2)** Line profiles of pixel intensity for immunofluorescence of D1R, D2R and TH in ICR mice and rats. The dotted white line for quantification of the pixel intensity is shown in the top panel. **(D)** Uneven distribution of D1R, D2R, and TH in the caudate of marmosets (coronal plane at  $\sim$ AP 3.3). **(E)** A magnified view of the caudate tail (CDt), including the poor zones (arrowheads). Note nerve bundles (arrows) crossing the striatum containing the poor zones. **(F)** Line profiles of the marmoset. Filled black circles represent the location of nerve bundles or large blood vessels. AST, amygdala striatal transition area; CDh, caudate head; CDt, caudate tail; Cx, cerebral cortex; ic, internal capsule; v, ventricle.

## DISCUSSION

The present study demonstrated that the rule of cellular correlation between dopamine receptor expression and projection pathways was conserved in the unusual part of the cStr where D1R-MSNs and D2R-MSNs are unevenly distributed. To the best of our knowledge, this is the first report which describes axonal projections from D1R-poor zones, although Gangarossa et al. (2013b) have reported that D2R-poor zone projected to SNpr and EP (refer to Valjent and Gangarossa, 2021). We identified the characteristic projections from the poor zones to SNpl *via* the direct pathway and to the caudal GP *via* the indirect pathway (Figures 6, 7 and Supplementary Figures 2–4). We have also elucidated that the electrophysiological properties of MSNs in the poor zones were similar to those observed in other striatal areas for most of the parameters evaluated in this study (Figure 4 and Table 3), and identified the poor zones in primates (Figure 9).

### Methodological Consideration

The present axonal tracing method may be considered to be limited, as the tracer deposit in the poor zones could be extremely small, causing incomplete labeling. Therefore, we cannot exclude the possibility of additional projections to other brain areas, not detected in the present study, or of potential differences in projections from two poor zones. However, even then, the projections that originated from a smaller population of MSNs in each poor zone, namely, the direct pathway in the D1R-poor zone or the indirect pathway in the D2R-poor zone, were successfully visualized. Thus, it is highly likely that characteristics of principal projections from the poor zones were correctly obtained, irrespective of the technical limitations. In addition, it should be mentioned that our electrophysiological experiments were also limited in regards to the sample size and the parameters analyzed. The present results simply showed that most of the basic membrane properties of MSNs in the poor zones were not significantly different from that of cdStr MSNs using *in vitro* preparations. However, as a significant difference was observed in the rheobase current, it could be also possible that there was some differentiation of detailed electrophysiological properties of MSNs in the poor zone. The differences in dopaminergic innervation and composition of interneurons (Miyamoto et al., 2019) can affect synaptic integration and plasticity. In addition, the axonal projections revealed by the microinjections of anterograde tracers were mainly derived from the D1R-poor zone. The possibility of differences in projections from the neurons in D1R- vs. D2R-poor zones cannot be excluded, although SNpl was a target for projections from both poor zones (Figure 7).

### Dual Pathway Neurons in Dopamine Receptor D1- and Dopamine Receptor D2-Poor Zones

In transgenic mice, uneven distribution of D1R and D2R expressing neurons in the cStr was reported (Gangarossa et al., 2013b, 2019; Miyamoto et al., 2019); the present study used wild type animals including C57BL/6J mice and our findings of the

locations of the unique zones and of cell-type composition were consistent with these previous reports (Figures 1, 2A–C).

Cellular distribution is not always precisely the same as the distribution of immunoreactivity, because the protein—visualized by immunohistochemistry, is localized at not only the soma but also in the dendrites and axons. To account for this, we performed *in situ* hybridization study and revealed the complementary distribution of *Drd1a* and *Drd2* expressing neurons in both D1R- and D2R-poor zones (Figure 3H). These findings suggest the possibility that the direct and indirect pathway neurons are unevenly distributed in the cvStr.

To address this question of uneven distribution of projection neurons, we initially performed a retrograde tracing study combined with immunohistochemistry. The proportion of retrogradely labeled striatonigral neurons, considered as direct pathway neurons, were significantly lower in the D1R-poor zone and significantly higher in the D2R-poor zone than other regions (Figures 5A–D). It is noteworthy that the estimated density of striatal neurons as observed by our large volume tracer injections is consistent with an early report (Rosen and Williams, 2001), suggesting that a large population of direct pathway neurons can be labeled and the differences in the labeled neuron density are not caused by the biased topographic distribution of projection neurons. In addition, the combined study of *in situ* hybridization with retrograde labeling showed that the retrogradely labeled direct pathway neurons expressed *Drd1a*, but not *Drd2* mRNA (Figures 5E,F). These findings indicated that the distribution of direct pathway neurons in the cvStr is highly biased toward the D2R-poor zone. Owing to the existence of axon collaterals of the direct pathway neurons in GP (Kawaguchi et al., 1990; Wu et al., 2000; Levesque and Parent, 2005; Fujiyama et al., 2011), it is difficult to label only the indirect pathway neurons using neural tracers. Nevertheless, our data suggested that D2R-neurons in the poor zones are likely to target GP as those in other striatal areas because the D1R-poor zone projection was denser in GP than in EP and/or SN (Figures 6, 7 and Supplementary Figure 2). In addition, retrograde tracer injection revealed that both caudal GP and cStr convergently projected to SNpl (Figures 7F–H). Anterograde tracing also suggested that the caudal GP is likely to constitute the indirect pathway of cStr including poor zones (Figure 6 and Supplementary Figure 2), as reported in primates (Amita and Hikosaka, 2019). Thus, the direct and indirect pathway neurons in the poor zones could form complementary circuitry, even though they were distributed unevenly. An assumption of the potential relationship between the poor zones and the striosome (patch)/matrix compartments may be implicated. However, in cvStr, typical striosome/matrix compartmentalization disappears (Miyamoto et al., 2018, 2019).

We also confirmed the preservation of D1R- and D2R-poor zones across age and species (Figures 8, 9); however, we did not conduct any experiments on their functional relevance. Thus, the necessity and/or significance of such unique regions is still unknown. In marmosets, the poor zones are likely to contain the ventral end of the putamen, the border region of putamen/CDt, as well as the rostral end of CDt. Alternatively, at least in this part of the striatum, the extent of CDt itself may spread out more dorsally than that of more caudal CDt which did not contain

the poor zones. A recent online atlas on marmosets<sup>2</sup> (Shimogori et al., 2018; Kita et al., 2021) supported the uneven distribution of D1R/D2R expressing cells (Drd1, ID#369-1 and #N-2; Drd2, ID #AA-2). The cStr, including poor zones, is innervated by the sensory cortices, which implies a possible relationship between sensory inputs and the poor zone development. However, this may not be the case. The poor zones were already present at P8, when behavioral reactions to tones or to visions were not yet elicited (Ehret, 1976; Huberman et al., 2008). Moreover, the poor zones were preserved in aged C57BL6/J mice even though they were generally hard of hearing (Zheng et al., 1999); however, sensory deprivation affects synaptic transmission in the sensory striatum (Mowery et al., 2017). Thus, the structure of the poor zones could develop and be maintained without sensory signals.

## The Caudal Striatum and the Poor Zone in Rodents and Primate

Recent studies with primates and rodents throw light on the functional aspect of the cStr. In the macaque monkey, the CDt, which is a long C-shaped structure of the ventral part of the caudate nucleus, has been reportedly involved in the distinct value coding (Kim and Hikosaka, 2013, 2015; Kim et al., 2014, 2017; Griggs et al., 2017). These findings can also be explained by the CDt receiving the distinct subpopulation of dopaminergic neurons in SNpc. Meanwhile, the poor zones in the common marmosets revealed here were located in approximately the most rostral end of the CDt. This part of the CDt is small; therefore, its neural connections and functions are still not clear. Contrastingly, Menegas et al. (2017, 2018) reported that the tail of the striatum in rodents is involved in saliency and aversion. In addition, the shape of the poor zones differed even in mice and rats (Figure 8). Thus, the anatomical and functional similarity of the poor zones and the tail of the striatum among species warrants further research.

## Functional Implications of the Poor Zone

We have reported that the main projection target of the cStr direct pathway, including the poor zones, was SNpl. The previous studies reported that cStr subregions receiving auditory cortical inputs project to the SNpl, whereas cStr subregions receiving visual cortical inputs project to the lateroventral SNpr (Kohno et al., 1984; Deniau et al., 1996). Such mesoscale topographic relationship was also reported in primates (Hedreen and DeLong, 1991). In turn, ventral SNpl is known to project to the superior colliculus (SC), inferior colliculus (IC), VPM, and so on; particularly, it innervates the sensory-related regions of the thalamus and midbrain (Yasui et al., 1991; Moriizumi et al., 1992; Takada, 1992; Cebrian et al., 2005). A recent study showed that SNpl was densely innervated by GABAergic neurons in the central amygdala (see also Supplementary Figure 4B), and the connection could relate to appetitive and aversive learning (Steinberg et al., 2020). Thus, the central amygdala and cStr have common characteristics on projections to SNpl, and on functional relevance to saliency and aversion. In addition, cStr

is innervated by sensory-related cortical areas: auditory, visual, secondary sensory, TeA, and perirhinal areas (Yeterian and Van Hoesen, 1978; Yeterian and Pandya, 1998; Hintiryan et al., 2016; Hunnicutt et al., 2016; Jiang and Kim, 2018). Recently, Li et al. (2021) reported that crescendo auditory stimuli, which mimic an approaching subject, induced freeze and flight responses in mice. Interestingly, corticostriatal innervation from the auditory cortex preferentially innervated D2R-neurons, in turn, excitation of these D2R-neurons increased freezing, although the precise relationship between the neural/behavioral responses and the poor zones are not reported. Taken together, cStr can contribute to the gating and integration of multimodalities of sensation *via* SN in rodents, similar to SN-subregion dependent information coding reported in primates (Yamamoto et al., 2012; Kim and Hikosaka, 2015; Yasuda and Hikosaka, 2015; Amita et al., 2020). However, it may be noteworthy that most of the neural activity data in primates have been obtained from a more caudal part of CDt. Our anterograde and retrograde tracing also suggested that the caudal GP is likely to constitute the indirect pathway of cStr including poor zones, which are projected to SNpl (Figures 6, 7), as reported in primates (Amita and Hikosaka, 2019). Furthermore, cdStr and poor zones tended to project slightly different parts of the SNpl (Figures 7A–E and Supplementary Figure 3), which suggests a potential functional differentiation between cdStr and the poor zones. The topographic projection from cStr has been previously reported (Foster et al., 2021), although the poor zones were not considered in the paper.

## Is the Poor Zone an Exception of the Striatum?

The classical model for the basal ganglia network suggests that normal function requires a balance of the direct and indirect pathway neurons mediated by D1R and D2R, respectively. The uneven distribution of the two MSNs population in the cStr raised a question regarding the balance between the direct and indirect pathway neurons. If the balance in the poor zones was as critical as other striatal areas, the two poor zones would share neural information with the aid of common inputs and/or mutual connections, or local circuitry within each zone, although our neural tracing experiments did not provide concrete evidence for these possibilities. Precise and detailed neural circuitry in these zones should be explored in future research. Whether D1R- and D2R-poor zones share common cortical inputs remains to be determined; if they do, two poor zones can work as one unit, like other striatal areas containing an equal number of D1R- and D2R-neurons. It is also possible that both poor zones could be innervated by different populations of cortical neurons. In other striatal regions, the cortical axons in the adjoining striatal areas originated from the adjacent but segregated cortical regions (Hooks et al., 2018; Ghosh and Zador, 2021). In such a case, two poor zones might communicate to compensate for the highly biased distribution of the direct and indirect pathway neurons, if they still need to work in a coordinated manner.

Alternatively, unlike motor- or limbic-related information processing in the striatum, these poor zones could work *via* either

<sup>2</sup><https://gene-atlas.brainminds.riken.jp>

the direct or indirect pathway. This view is supported by recent research that showed highly biased corticostriatal innervation onto D2R-neurons from the auditory cortex (Li et al., 2021). In such an event, lesser dopaminergic innervation specifically observed in the poor zones, which is likely to be from the SNpl (Watabe-Uchida et al., 2012; Menegas et al., 2015; Jiang and Kim, 2018; Poulin et al., 2018) could also relate to such unusual striatal circuitry. Because it is suggested that the nucleus accumbens, a part of the limbic system, also contains a poor zone-like structure (Gangarossa et al., 2013a; Petryszyn et al., 2017), the unique circuit may not only relate to the sensory system. Furthermore, to determine whether the poor zones and cdStr are functionally differentiated and whether the cStr is a counterpart of the primate CDt, neural tracing and functional recording/imaging in extremely fine scales are required, which will help to understand the two pathways beyond the current concept.

## DATA AVAILABILITY STATEMENT

The raw data supporting the conclusions of this article will be made available by the authors, without undue reservation.

## ETHICS STATEMENT

The animal study was reviewed and approved by the Committee for Animal Care and Use of Doshisha University; the Animal Care and Use Committee of Hokkaido University; and the Animal Welfare and Animal Care Committee of the Primate Research Institute of Kyoto University.

## AUTHOR CONTRIBUTIONS

All authors: full access to the data in the study and take responsibility for the integrity of the data and

## REFERENCES

- Albin, R. L., Young, A. B., and Penney, J. B. (1989). The functional anatomy of basal ganglia disorders. *Trends Neurosci.* 12, 366–375.
- Alexander, G. E., and Crutcher, M. D. (1990). Functional architecture of basal ganglia circuits: neural substrates of parallel processing. *Trends Neurosci.* 13, 266–271.
- Alexander, G. E., DeLong, M. R., and Strick, P. L. (1986). Parallel organization of functionally segregated circuits linking basal ganglia and cortex. *Annu. Rev. Neurosci.* 9, 357–381.
- Amita, H., and Hikosaka, O. (2019). Indirect pathway from caudate tail mediates rejection of bad objects in periphery. *Sci. Adv.* 5:eaaw9297. doi: 10.1126/sciadv.aaw9297
- Amita, H., Kim, H. F., Inoue, K. I., Takada, M., and Hikosaka, O. (2020). Optogenetic manipulation of a value-coding pathway from the primate caudate tail facilitates saccadic gaze shift. *Nat. Commun.* 11:1876. doi: 10.1038/s41467-020-15802-y
- Brown, V. J., Desimone, R., and Mishkin, M. (1995). Responses of cells in the tail of the caudate nucleus during visual discrimination learning. *J. Neurophysiol.* 74, 1083–1094. doi: 10.1152/jn.1995.74.3.1083
- Caan, W., Perrett, D. I., and Rolls, E. T. (1984). Responses of striatal neurons in the behaving monkey. 2. Visual processing in the caudal neostriatum. *Brain Res.* 290, 53–65. doi: 10.1016/0006-8993(84)90735-2

the accuracy of the data analysis, writing – review and editing. FF and FKar: conceptualization, supervision, and funding acquisition. FKar, YH, and KO: methodology. KO, FKar, FKad, YH, and FF: investigation. KO, FKad, FKar, and YH: formal analysis. K-II and MT: resources. KO, FF, and FKar: writing – original draft. KO and FKar: visualization.

## FUNDING

This study was funded by Grants-in-Aid from the Ministry of Education, Culture, Sports, Science, and Technology (MEXT) and Japan Society for the Promotion of Science (JSPS) for Scientific Research (20H03549 to FF) for Exploratory Research (20K20671 to FF) and for Scientific Researches on Innovative Areas “Hyper-Adaptability” (20H05484 to FF), and for Scientific Researches on Innovative Areas “Adaptation Circuit Census” (21H05241 to FF and to FKar).

## ACKNOWLEDGMENTS

We thank H. Hioki and S. Okamoto for their suggestions on *in situ* hybridization. We thank S. Takahashi and T. Higashiyama for their helpful insights. We also extend our gratitude to Y. Sakurai for supervising the study and for his kind encouragement.

## SUPPLEMENTARY MATERIAL

The Supplementary Material for this article can be found online at: <https://www.frontiersin.org/articles/10.3389/fnana.2022.809446/full#supplementary-material>

- Calabresi, P., Picconi, B., Tozzi, A., Ghiglieri, V., and Di Filippo, M. (2014). Direct and indirect pathways of basal ganglia: a critical reappraisal. *Nat. Neurosci.* 17, 1022–1030. doi: 10.1038/nn.3743
- Cebrian, C., Parent, A., and Prensa, L. (2005). Patterns of axonal branching of neurons of the substantia nigra pars reticulata and pars lateralis in the rat. *J. Comparat. Neurol.* 492, 349–369. doi: 10.1002/cne.20741
- Cui, G., Jun, S. B., Jin, X., Pham, M. D., Vogel, S. S., Lovinger, D. M., et al. (2013). Concurrent activation of striatal direct and indirect pathways during action initiation. *Nature* 494, 238–242. doi: 10.1038/nature11846
- Deniau, J. M., Menetrey, A., and Charpier, S. (1996). The lamellar organization of the rat substantia nigra pars reticulata: segregated patterns of striatal afferents and relationship to the topography of corticostriatal projections. *Neuroscience* 73, 761–781. doi: 10.1016/0306-4522(96)00088-7
- Ehret, G. (1976). Development of absolute auditory thresholds in the house mouse (*Mus musculus*). *J. Am. Audiol. Soc.* 1, 179–184.
- Foster, N. N., Barry, J., Korobkova, L., Garcia, L., Gao, L., Becerra, M., et al. (2021). The mouse cortico-basal ganglia-thalamic network. *Nature* 598, 188–194. doi: 10.1038/s41586-021-03993-3
- Friend, D. M., and Kravitz, A. V. (2014). Working together: basal ganglia pathways in action selection. *Trends Neurosci.* 37, 301–303. doi: 10.1016/j.tins.2014.04.004
- Fujiyama, F., Sohn, J., Nakano, T., Furuta, T., Nakamura, K. C., Matsuda, W., et al. (2011). Exclusive and common targets of neostriatofugal projections of

- rat striosome neurons: a single neuron-tracing study using a viral vector. *Eur. J. Neurosci.* 33, 668–677. doi: 10.1111/j.1460-9568.2010.07564.x
- Furuta, T., Kaneko, T., and Deschenes, M. (2009). Septal neurons in barrel cortex derive their receptive field input from the lemniscal pathway. *J. Neurosci.: Off. J. Soc. Neurosci.* 29, 4089–4095. doi: 10.1523/JNEUROSCI.5393-08.2009
- Gangarossa, G., Castell, L., Castro, L., Tarot, P., Veyrunes, F., Vincent, P., et al. (2019). Contrasting patterns of ERK activation in the tail of the striatum in response to aversive and rewarding signals. *J. Neurochem.* 151, 204–226. doi: 10.1111/jnc.14804
- Gangarossa, G., Espallergues, J., Mailly, P., De Bundel, D., de Kerchove d'Exaerde, A., Herve, D., et al. (2013b). Spatial distribution of D1R- and D2R-expressing medium-sized spiny neurons differs along the rostro-caudal axis of the mouse dorsal striatum. *Front. Neural Circuits* 7:124. doi: 10.3389/fncir.2013.00124
- Gangarossa, G., Espallergues, J., de Kerchove d'Exaerde, A., Mestikawy, S. E., Gerfen, C. R., Herve, D., et al. (2013a). Distribution and compartmental organization of GABAergic medium-sized spiny neurons in the mouse nucleus accumbens. *Front. Neural Circuits* 7:22. doi: 10.3389/fncir.2013.00022
- Ge, S. N., Ma, Y. F., Hioki, H., Wei, Y. Y., Kaneko, T., Mizuno, N., et al. (2010). Coexpression of VGLUT1 and VGLUT2 in trigeminothalamic projection neurons in the principal sensory trigeminal nucleus of the rat. *J. Comparat. Neurol.* 518, 3149–3168. doi: 10.1002/cne.22389
- Gerfen, C. R. (1989). The neostriatal mosaic: striatal patch-matrix organization is related to cortical lamination. *Science* 246, 385–388. doi: 10.1126/science.2799392
- Ghosh, S., and Zador, A. M. (2021). Corticostriatal plasticity established by initial learning persists after behavioral reversal. *eNeuro* 8:ENEURO.0209-20.2021. doi: 10.1523/ENEURO.0209-20.2021
- Graybiel, A. M. (1990). Neurotransmitters and neuromodulators in the basal ganglia. *Trends Neurosci.* 13, 244–254. doi: 10.1016/0166-2236(90)90104-i
- Griggs, W. S., Kim, H. F., Ghazizadeh, A., Gabriela Costello, M., Wall, K. M., and Hikosaka, O. (2017). Flexible and stable value coding areas in caudate head and tail receive anatomically distinct cortical and subcortical inputs. *Front. Neuroanat.* 11:106. doi: 10.3389/fnana.2017.00106
- Hedreen, J. C., and DeLong, M. R. (1991). Organization of striatopallidal, striatonigral, and nigrostriatal projections in the macaque. *J. Comparat. Neurol.* 304, 569–595. doi: 10.1002/cne.903040406
- Hikosaka, O., Takikawa, Y., and Kawagoe, R. (2000). Role of the basal ganglia in the control of purposive saccadic eye movements. *Physiol. Rev.* 80, 953–978. doi: 10.1152/physrev.2000.80.3.953
- Hintiryan, H., Foster, N. N., Bowman, I., Bay, M., Song, M. Y., Gou, L., et al. (2016). The mouse cortico-striatal projectome. *Nat. Neurosci.* 19, 1100–1114. doi: 10.1038/nn.4332
- Hioki, H., Nakamura, H., Ma, Y. F., Konno, M., Hayakawa, T., Nakamura, K. C., et al. (2010). Vesicular glutamate transporter 3-expressing nonserotonergic projection neurons constitute a subregion in the rat midbrain raphe nuclei. *J. Comparat. Neurol.* 518, 668–686. doi: 10.1002/cne.22237
- Hooks, B. M., Papale, A. E., Paletzki, R. F., Feroze, M. W., Eastwood, B. S., Couey, J. J., et al. (2018). Topographic precision in sensory and motor corticostriatal projections varies across cell type and cortical area. *Nat. Commun.* 9:3549.
- Huberman, A. D., Feller, M. B., and Chapman, B. (2008). Mechanisms underlying development of visual maps and receptive fields. *Annu. Rev. Neurosci.* 31, 479–509. doi: 10.1146/annurev.neuro.31.060407.125533
- Hunnicutt, B. J., Jongbloets, B. C., Birdsong, W. T., Gertz, K. J., Zhong, H., and Mao, T. (2016). A comprehensive excitatory input map of the striatum reveals novel functional organization. *eLife* 5:e19103. doi: 10.7554/eLife.19103
- Isomura, Y., Takekawa, T., Harukuni, R., Handa, T., Aizawa, H., Takada, M., et al. (2013). Reward-modulated motor information in identified striatum neurons. *J. Neurosci.: Off. J. Soc. Neurosci.* 33, 10209–10220. doi: 10.1523/JNEUROSCI.0381-13.2013
- Jiang, H., and Kim, H. F. (2018). Anatomical inputs from the sensory and value structures to the tail of the rat striatum. *Front. Neuroanat.* 12:30. doi: 10.3389/fnana.2018.00030
- Karube, F., Takahashi, S., Kobayashi, K., and Fujiyama, F. (2019). Motor cortex can directly drive the globus pallidus neurons in a projection neuron type-dependent manner in the rat. *eLife* 8:e49511. doi: 10.7554/eLife.49511
- Kawaguchi, Y., Wilson, C. J., and Emson, P. C. (1990). Projection subtypes of rat neostriatal matrix cells revealed by intracellular injection of biocytin. *J. Neurosci.: Off. J. Soc. Neurosci.* 10, 3421–3438. doi: 10.1523/JNEUROSCI.10-10-03421.1990
- Kim, H. F., Amita, H., and Hikosaka, O. (2017). Indirect pathway of caudal basal ganglia for rejection of valueless visual objects. *Neuron* 94, 920.e923–930.e923. doi: 10.1016/j.neuron.2017.04.033
- Kim, H. F., Ghazizadeh, A., and Hikosaka, O. (2014). Separate groups of dopamine neurons innervate caudate head and tail encoding flexible and stable value memories. *Front. Neuroanat.* 8:120. doi: 10.3389/fnana.2014.00120
- Kim, H. F., and Hikosaka, O. (2013). Distinct basal ganglia circuits controlling behaviors guided by flexible and stable values. *Neuron* 79, 1001–1010. doi: 10.1016/j.neuron.2013.06.044
- Kim, H. F., and Hikosaka, O. (2015). Parallel basal ganglia circuits for voluntary and automatic behaviour to reach rewards. *Brain: J. Neurol.* 138, 1776–1800. doi: 10.1093/brain/awv134
- Kita, Y., Nishibe, H., Wang, Y., Hashikawa, T., Kikuchi, S. S., Mami, U., et al. (2021). Cellular-resolution gene expression profiling in the neonatal marmoset brain reveals dynamic species- and region-specific differences. *Proc. Natl. Acad. Sci. U.S.A.* 118:e2020125118. doi: 10.1073/pnas.2020125118
- Kohno, J., Shiosaka, S., Shinoda, K., Inagaki, S., and Tohyama, M. (1984). Two distinct strio-nigral substance P pathways in the rat: an experimental immunohistochemical study. *Brain Res.* 308, 309–317. doi: 10.1016/0006-8993(84)91070-9
- Krajcsik, R. N., Macey-Dare, A., van Heusden, F., Ebrahimjee, F., and Ellender, T. J. (2019). Dynamic postnatal development of the cellular and circuit properties of striatal D1 and D2 spiny projection neurons. *J. Physiol.* 597, 5265–5293. doi: 10.1113/JP278416
- Kreitzer, A. C., and Malenka, R. C. (2008). Striatal plasticity and basal ganglia circuit function. *Neuron* 60, 543–554. doi: 10.1016/j.neuron.2008.11.005
- Kuramoto, E., Furuta, T., Nakamura, K. C., Unzai, T., Hioki, H., and Kaneko, T. (2009). Two types of thalamocortical projections from the motor thalamic nuclei of the rat: a single neuron-tracing study using viral vectors. *Cerebral Cortex* 19, 2065–2077. doi: 10.1093/cercor/bhn231
- Lança, A. J., Boyd, S., Kolb, B. E., and Van Der Kooy, D. (1986). The development of a Patchy organization of the rat striatum. *Dev. Brain Res.* 27, 1–10. doi: 10.1016/0165-3806(86)90226-9
- Levesque, M., and Parent, A. (2005). The striatofugal fiber system in primates: a reevaluation of its organization based on single-axon tracing studies. *Proc. Natl. Acad. Sci. U.S.A.* 102, 11888–11893. doi: 10.1073/pnas.0502710102
- Li, Z., Wei, J.-X., Zhang, G.-W., Huang, J. J., Zingg, B., Wang, X., et al. (2021). Corticostriatal control of defence behavior in mice induced by auditory looming cues. *Nat. Commun.* 12:1040. doi: 10.1038/s41467-021-21248-7
- Ma, Y., Hioki, H., Konno, M., Pan, S., Nakamura, H., Nakamura, K. C., et al. (2011). Expression of gap junction protein connexin36 in multiple subtypes of GABAergic neurons in adult rat somatosensory cortex. *Cerebral Cortex* 21, 2639–2649. doi: 10.1093/cercor/bhr051
- Menegas, W., Akiti, K., Amo, R., Uchida, N., and Watabe-Uchida, M. (2018). Dopamine neurons projecting to the posterior striatum reinforce avoidance of threatening stimuli. *Nat. Neurosci.* 21, 1421–1430. doi: 10.1038/s41593-018-0222-1
- Menegas, W., Babayan, B. M., Uchida, N., and Watabe-Uchida, M. (2017). Opposite initialization to novel cues in dopamine signaling in ventral and posterior striatum in mice. *eLife* 6:e21886. doi: 10.7554/eLife.21886
- Menegas, W., Bergan, J. F., Ogawa, S. K., Isogai, Y., Umadevi Venkataraju, K., Osten, P., et al. (2015). Dopamine neurons projecting to the posterior striatum form an anatomically distinct subclass. *eLife* 4:e10032. doi: 10.7554/eLife.10032
- Miyamoto, Y., Katayama, S., Shigematsu, N., Nishi, A., and Fukuda, T. (2018). Striosome-based map of the mouse striatum that is conformable to both cortical afferent topography and uneven distributions of dopamine D1 and D2 receptor-expressing cells. *Brain Struct. Funct.* 223, 4275–4291. doi: 10.1007/s00429-018-1749-3
- Miyamoto, Y., Nagayoshi, I., Nishi, A., and Fukuda, T. (2019). Three divisions of the mouse caudal striatum differ in the proportions of dopamine D1 and D2 receptor-expressing cells, distribution of dopaminergic axons, and composition of cholinergic and GABAergic interneurons. *Brain Struct. Funct.* 224, 2703–2716. doi: 10.1007/s00429-019-01928-3
- Moriizumi, T., Leduc-Cross, B., Wu, J. Y., and Hattori, T. (1992). Separate neuronal populations of the rat substantia nigra pars lateralis with distinct projection

- sites and transmitter phenotypes. *Neuroscience* 46, 711–720. doi: 10.1016/0306-4522(92)90157-w
- Mowery, T. M., Penikis, K. B., Young, S. K., Ferrer, C. E., Kotak, V. C., and Sanes, D. H. (2017). The sensory striatum is permanently impaired by transient developmental deprivation. *Cell Rep.* 19, 2462–2468. doi: 10.1016/j.celrep.2017.05.083
- Nambu, A. (2008). Seven problems on the basal ganglia. *Curr. Opin. Neurobiol.* 18, 595–604. doi: 10.1016/j.conb.2008.11.001
- Ogata, K., Karube, F., Hirai, Y., and Fujiyama, F. (2018). *The Unique Distribution of D1 and D2 Dopamine Receptors in the Lateral Caudal Striatum of Rodents*. Annual Meeting of Society for Neuroscience 2018. Abstract number 146.14. In San Diego, November 3–7. San Diego, CA.
- Paxinos, G., and Franklin, K. B. (2013). *The Mouse Brain in Stereotaxic Coordinates*, 4th Edn. Amsterdam: Elsevier.
- Peak, J., Hart, G., and Balleine, B. W. (2019). From learning to action: the integration of dorsal striatal input and output pathways in instrumental conditioning. *Eur. J. Neurosci.* 49, 658–671. doi: 10.1111/ejn.13964
- Petryszyn, S., Sánchez, M. G., Gagnon, D., Beaulieu, J. M., Parent, A., and Parent, M. (2017). A dense cluster of D1+ cells in the mouse nucleus accumbens. *Synapse* 71, 51–54. doi: 10.1002/syn.21946
- Poulin, J. F., Caronia, G., Hofer, C., Cui, Q., Helm, B., Ramakrishnan, C., et al. (2018). Mapping projections of molecularly defined dopamine neuron subtypes using intersectional genetic approaches. *Nat. Neurosci.* 21, 1260–1271. doi: 10.1038/s41593-018-0203-4
- Redgrave, P., Vautrelle, N., and Reynolds, J. N. (2011). Functional properties of the basal ganglia's re-entrant loop architecture: selection and reinforcement. *Neuroscience* 198, 138–151. doi: 10.1016/j.neuroscience.2011.07.060
- Rosen, G. D., and Williams, R. W. (2001). Complex trait analysis of the mouse striatum: independent QTLs modulate volume and neuron number. *BMC Neurosci.* 2:5. doi: 10.1186/1471-2202-2-5
- Saint-Cyr, J. A., Ungerleider, L. G., and Desimone, R. (1990). Organization of visual cortical inputs to the striatum and subsequent outputs to the pallido-nigral complex in the monkey. *J. Comparat. Neurol.* 298, 129–156. doi: 10.1002/cne.902980202
- Schindelin, J., Arganda-Carreras, I., Frise, E., Kaynig, V., Longair, M., Pietzsch, T., et al. (2012). Fiji: an open-source platform for biological-image analysis. *Nat. Methods* 9, 676–682. doi: 10.1038/nmeth.2019
- Selemon, L. D., and Goldman-Rakic, P. S. (1990). Topographic intermingling of striatonigral and striatopallidal neurons in the rhesus monkey. *J. Comparat. Neurol.* 297, 359–376. doi: 10.1002/cne.902970304
- Shepherd, G. M. (2013). Corticostriatal connectivity and its role in disease. *Nat. Rev. Neurosci.* 14, 278–291.
- Shimogori, T., Abe, A., Go, Y., Hashikawa, T., Kishi, N., Kikuchi, S. S., et al. (2018). Digital gene atlas of neonate common marmoset brain. *Neurosci. Res.* 128, 1–13. doi: 10.1016/j.neures.2017.10.009
- Shipp, S. (2016). The functional logic of corticostriatal connections. *Brain Struct. Funct.* 222, 669–706. doi: 10.1007/s00429-016-1250-9
- Sonntag, M., Englitz, B., Kopp-Scheinpflug, C., and Rubsamen, R. (2009). Early postnatal development of spontaneous and acoustically evoked discharge activity of principal cells of the medial nucleus of the trapezoid body: an *in vivo* study in mice. *J. Neurosci.* 29, 9510–9520. doi: 10.1523/JNEUROSCI.1377-09.2009
- Steinberg, E. E., Gore, F., Heifets, B. D., Taylor, M. D., Norville, Z. C., Beier, K. T., et al. (2020). Amygdala-midbrain connections modulate appetitive and aversive learning. *Neuron* 106, 1026–1043. doi: 10.1016/j.neuron.2020.03.016
- Takada, M. (1992). The lateroposterior thalamic nucleus and substantia nigra pars lateralis: origin of dual innervation over the visual system and basal ganglia. *Neurosci. Lett.* 139, 153–156. doi: 10.1016/0304-3940(92)90540-n
- Tinterri, A., Menardy, F., Diana, M. A., Lokmane, L., Keita, M., Coulpier, F., et al. (2018). Active intermixing of indirect and direct neurons builds the striatal mosaic. *Nat. Commun.* 9:4725. doi: 10.1038/s41467-018-07171-4
- Valjent, E., and Gangarossa, G. (2021). The tail of the striatum: from anatomy to connectivity and function. *Trends Neurosci.* 44, 203–214. doi: 10.1016/j.tins.2020.10.016
- Watabe-Uchida, M., Zhu, L., Ogawa, S. K., Vamanrao, A., and Uchida, N. (2012). Whole-brain mapping of direct inputs to midbrain dopamine neurons. *Neuron* 74, 858–873. doi: 10.1016/j.neuron.2012.03.017
- Wu, Y., Richard, S., and Parent, A. (2000). The organization of the striatal output system: a single-cell juxtacellular labeling study in the rat. *Neurosci. Res.* 38, 49–62. doi: 10.1016/s0168-0102(00)00140-1
- Xiong, Q., Znamenskiy, P., and Zador, A. M. (2015). Selective corticostriatal plasticity during acquisition of an auditory discrimination task. *Nature* 521, 348–351. doi: 10.1038/nature14225
- Yamamoto, S., Monosov, I. E., Yasuda, M., and Hikosaka, O. (2012). What and where information in the caudate tail guides saccades to visual objects. *J. Neurosci.: Off. J. Soc. Neurosci.* 32, 11005–11016. doi: 10.1523/JNEUROSCI.0828-12.2012
- Yasuda, M., and Hikosaka, O. (2015). Functional territories in primate substantia nigra pars reticulata separately signaling stable and flexible values. *J. Neurophysiol.* 113, 1681–1696. doi: 10.1152/jn.00674.2014
- Yasui, Y., Nakano, K., Kayahara, T., and Mizuno, N. (1991). Non-dopaminergic projections from the substantia nigra pars lateralis to the inferior colliculus in the rat. *Brain Res.* 559, 139–144. doi: 10.1016/0006-8993(91)90296-8
- Yeterian, E. H., and Pandya, D. N. (1998). Corticostriatal connections of the superior temporal region in rhesus monkeys. *J. Comparat. Neurol.* 399, 384–402.
- Yeterian, E. H., and Van Hoesen, G. W. (1978). Cortico-striate projections in the rhesus monkey: the organization of certain cortico-caudate connections. *Brain Res.* 139, 43–63. doi: 10.1016/0006-8993(78)90059-8
- Zheng, Q. Y., Johnson, K. R., and Erway, L. C. (1999). Assessment of hearing in 80 inbred strains of mice by ABR threshold analyses. *Hear. Res.* 130, 94–107.

**Conflict of Interest:** The authors declare that the research was conducted in the absence of any commercial or financial relationships that could be construed as a potential conflict of interest.

**Publisher's Note:** All claims expressed in this article are solely those of the authors and do not necessarily represent those of their affiliated organizations, or those of the publisher, the editors and the reviewers. Any product that may be evaluated in this article, or claim that may be made by its manufacturer, is not guaranteed or endorsed by the publisher.

Copyright © 2022 Ogata, Kadono, Hirai, Inoue, Takada, Karube and Fujiyama. This is an open-access article distributed under the terms of the Creative Commons Attribution License (CC BY). The use, distribution or reproduction in other forums is permitted, provided the original author(s) and the copyright owner(s) are credited and that the original publication in this journal is cited, in accordance with accepted academic practice. No use, distribution or reproduction is permitted which does not comply with these terms.